Construction and Building Materials 457 (2024) 139165

Contents lists available at ScienceDirect

Construction and Building Materials

journal homepage: www.elsevier.com/locate/conbuildmat

Enhancing mortar composite matrices with three-dimensional auxetic truss lattice materials for reinforced concrete structures

Thomas Vitalis [a], Andrew Gross [b], George Tzortzinis [c], Brian Schagen [a], Simos Gerasimidis [a,*]

[a] Department of Civil & Environmental Engineering, University of Massachusetts Amherst, Amherst, 01003, MA, USA
[b] Department of Mechanical Engineering, University of South Carolina, Columbia, 29208, SC, USA
[c] Institute of Lightweight Engineering and Polymer Technology, Technische Universität Dresden, Dresden, 01187, Germany

ARTICLE INFO

Keywords:
Composite materials
Confinement
Auxetics
Reinforcement
Civil infrastructure

ABSTRACT

Auxetic architected materials have been at the forefront of developing materials with a wide range of negative Poisson's ratios, tunable stiffness, and high ductility due to their novel deformation under uniaxial compression. Despite that, the adoption of auxetic materials in load-bearing applications has been challenged by the requirement that their bulk modulus is significantly less than that of the fully dense parent material. In this paper, we study whether using the same mechanism that provides a negative Poisson's ratio can be mimicked in an interpenetrating phase composite to enhance its matrix's peak strength and mechanical behavior. In this case, a brittle matrix can be enhanced with a small volumetric fraction of an auxetic truss lattice. The auxetic phase behaves as reinforcement, increasing the hydrostatic compression and confinement in the matrix caused by the externally applied load and bridging matrix cracking. Our work is focused on rapidly prototyping composites using a concrete/mortar matrix with 15-5 PH stainless steel auxetic truss lattice reinforcement. The families of re-entrant bowtie and double pyramid truss lattices were manufactured using laser powder bed fusion to study the effects of increasing the confinement pressure when embedded in composite mortar/steel matrices. The results of the experimental program with LPBF-manufactured truss lattices tested under axial compression embedded in mortar composites are presented and discussed. Analytical modeling is used to decompose the effects of stiffness and Poisson's ratio on the confining pressure generated by the reinforcing phase. Numerical results on a perfectly bonded periodic unit cell of the composite material are illustrated, presenting the auxetic confinement pressures for different characteristic angles of the architectures with a maximum increase in confining pressure of 34.4%. Our findings reveal significant enhancements in ductility and peak strength using the proposed scheme, with gains reaching up to 240% and 165%, respectively, when compared to conventionally confined specimens and a non-rule-of-mixtures behavior in the composite.

1. Introduction

The advances that took place during the last two decades in the field of advanced manufacturing [1–4], robotics [5], material science [6–8], software & hardware development have enabled researchers to develop architected materials and meta-materials with intentionally superior mechanical [9–12] as well as electromagnetic properties [13,14]. The exploration of extraordinary properties in materials such as negative Poisson's ratio materials [9,15–17], high strength from nano-scale materials [18–20], hierarchical multi-scale materials [21–23], and tunable bandgap materials [13,24] has been significantly accelerated by progress in additive manufacturing methods in the last decade. At the same time, the widespread adoption of additive manufacturing has led to lowering the manufacturing cost per part [25], bolstering rapid prototyping for industrial and research applications, and enabling engineers to manufacture intricate mechanical parts with superior mechanical properties that were previously unattainable.

In the face of growing infrastructure challenges, accelerated by the action of decaying infrastructure and climate change, the adoption of the innovations seen in the aforementioned fields has been sluggish in the field of civil infrastructure. Specifically, almost 40% of the total yearly energy-related CO_2 emissions originate from civil infrastructure [26]. The yearly investments in the sector were estimated to be around 237 billion USD in 2021 [27]. However, the examples of advanced manufacturing methods applied in the construction industry are still very limited, mostly focusing on concrete 3D printing [28–33], printing of non-ordinary Portland concrete mixes [34,35], and proof-of-concept applications [36,37]. The adoption of architected materials in civil infrastructure and specifically in the design and detailing

* Corresponding author.
E-mail address: sgerasimidis@umass.edu (S. Gerasimidis).

https://doi.org/10.1016/j.conbuildmat.2024.139165
Received 23 August 2024; Received in revised form 11 October 2024; Accepted 9 November 2024

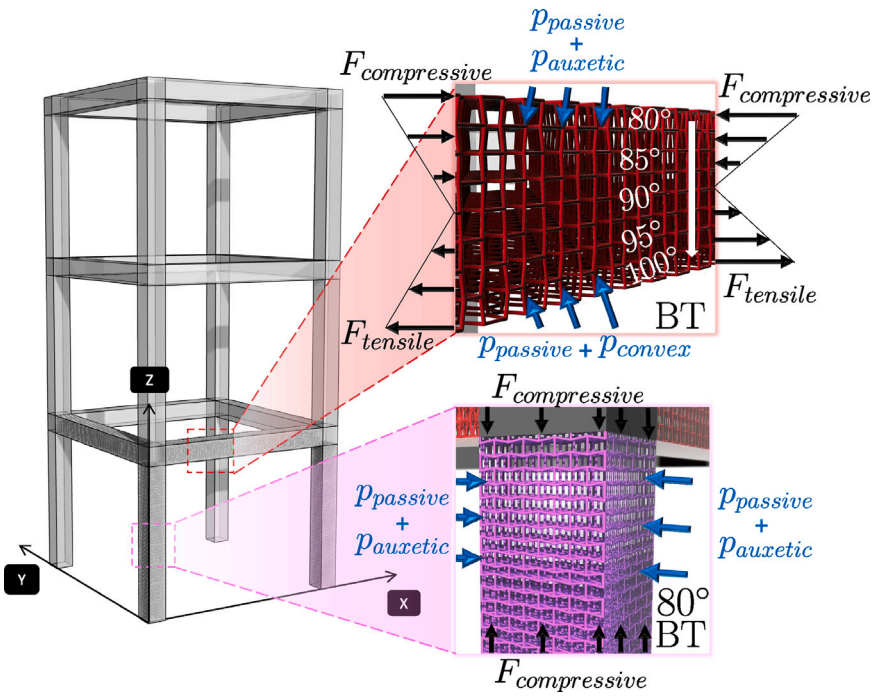

Fig. 1. Conceptual schematic illustrating the increase in confinement pressure with the utilization of auxetic reinforced concrete in a reinforced concrete frame. The columns are designed using the $\theta = 80°$ bowtie geometry throughout their height [37]. The beams are designed with a gradual gradient in their angles using both auxetic and convex honeycomb architectures with a transition from 80° to 100°, to harness the pressure generated by auxetic and convex unit cells in the compressive and tensile zones accordingly.

of structural members has been challenged so far by the high cost when compared to traditional methods [25] and the intricacy of the interplaying mechanics involved in such an endeavor, that require comprehensive studying of the composite mechanical behavior. Few studies of architected material reinforced concrete elements exist [37–41], however, without presenting a comprehensive experimental study of different architectures and varying geometrical features.

In terms of its elastic properties, a steel-reinforced concrete member can be studied as a composite section consisting of two phases with different elastic moduli. The soft phase is the concrete/mortar phase, while the hard phase is the reinforcing architecture, preferably made out of steel to achieve high elastic contrast with the concrete/mortar. In the elastic region and prior to concrete cracking, strain compatibility can be assumed for both materials. Post-cracking stress relaxation is present in the concrete phase until the yielding of the reinforcing steel. In the case of reinforced concrete beams, the reinforcing steel receives the tensile stresses in the tension zone, while compressive reinforcement reduces cracks and increases stiffness. In the case of reinforced concrete columns, the longitudinal reinforcing steel provides axial stiffness, while the transverse reinforcement provides shear resistance and lateral confinement to the expansion of the confined concrete core. The flow of forces is assumed to follow the strut-and-tie model based on Ritter's [42] and Mörsch's [43] original truss model approach, which was later improved by Leonhardt, Rusch, Kupfer, and others [44]. Further study of the same model, including a rational design considering plasticity, was expanded by Marti, Mueller, and Schlaich [44,45].

Confinement of reinforced concrete increases the strength and ductility of reinforced concrete columns and beams. It was first introduced by Richart et al. [46], with Kent and Park [47] being the first to develop analytical models based on large-scale experiments for beams and with Sheikh & Uzumeri [48], Priestley, Park & Scott [49] and Mander [50,51] creating analytical models for columns and Saatcioglu, Razvi [52] and an abundance of other researchers who further expanded this work. The ACI Code was largely based on these publications, which radically changed how structural elements are designed in both seismic and non-seismic areas.

The same mechanism that provides stiffness, reduces cracking, and supplies confinement to reinforced concrete members can be mimicked with architected materials and further optimized and tailored to harness the unique properties of architected material unit cells. Auxetic materials, which are a class of elastic metamaterials, are cellular materials that possess the extraordinary ability to laterally contract and densify more rapidly than conventional materials under the application of compressive loads (conversely, auxetics expand laterally when tension is applied to them). This unique behavior arises due to their unique architectures [17], for which the geometric and topological conditions have become well known [53]. The adoption of auxetic materials inside interpenetrating phase composites (IPCs) has been proven to generate greater confining pressure than their non-auxetic counterparts, thus increasing the load-bearing capacity of IPCs undergoing large deformations [37]. The enhancement in confining pressure that occurs inside IPCs can be explained by the superposition of passive confinement generated by the reaction of the reinforcing phase resisting the expansion of the concrete matrix and the auxetic confinement generated by the predisposition of the auxetic reinforcing phase to contract laterally. From a civil infrastructure perspective, this mechanism can be harnessed by the adoption of auxetic reinforcement to improve the confinement of a concrete column or beam (Fig. 1). The fabrication of such truss reinforcement in the structure scale can be enabled via robotic manufacturing [54]. The design of joints able to rigidly connect such structural elements could utilize topology optimization methods [55]. Additional benefits, such as enhanced redundancy of the distributed reinforcement and crack bridging, may occur from the adoption of architected materials as concrete reinforcement, depending on the architecture used.

In this paper, we study the compressive behavior of auxetic architected material reinforced interpenetrating phase composites (IPCs) with 2 different families of auxetic architectures and 3 different sets of characteristic geometric parameters for each architecture. This work aims to investigate the various mechanical behaviors that arise with the tunability of auxetics inside IPCs through additive manufacturing and rapid prototyping for potential future applications in reinforced concrete civil infrastructure. First, through the means of computational

and analytical modeling, we identify the candidate auxetic designs that generate the largest increase in confining pressures. Secondly, we design and manufacture the proposed architectures using laser powder bed fusion and a precipitation hardening 15–5 pre-alloyed steel powder. We determine a mix design with adequate rheology to flow and compact inside the reinforcement phase satisfactorily to fabricate composite experimental specimens. The prepared IPC specimens are tested under axial compression, and their stress–strain curves and deformation modes are presented for each architecture. Finite element computations are used to verify the experimental work, and additional models using conventional reinforced concrete designs are compared using the same volume fraction of steel as in the IPCs. Overall, a comparison of the enhancement of the peak stresses and ductilities of auxetically confined concrete is provided for three different geometrical configurations with varying elastic properties and Poisson's ratios from two re-entrant auxetic families and conventional confinement techniques. Based on the experimental work, suggestions for future directions are discussed towards adopting architected materials in structural elements of reinforced concrete civil infrastructure.

2. Bare auxetic linear behavior and analytical prediction of confinement

To design auxetic material IPCs, a variety of novel auxetic architectures from the literature was considered [16,56–66]. The selection of the most appropriate unit cell candidates was based on the manufacturability (additive manufacturing on the small scale [17] and feasibility of robotic upscaling of the manufacturing process), the ability to generate unit cells with a wide range of elastic properties and Poisson's ratios by varying the geometrical features of the architecture, and the low intricacy, nodal connectivity and openness of the unit cell geometry for concrete/mortar to easily flow through the truss lattice and achieve satisfactory compaction of the matrix phase.

After considering these criteria, the two re-entrant families of the auxetic bowtie honeycomb (BT) and double pyramid (DP) were selected, with nodal connectivities of Z = 5 for bowties and Z = 5.333 for double pyramids. Both unit cells are tetragonal, with the bowtie having equal strut lengths L for all the interior struts of its architecture and the double pyramid containing two groups of struts with lengths of L_1 and L_2, with $L_1 > L_2$ [17]. For the numerical investigation and manufacturing of the IPCs, a low unit cell relative density of $\rho^* = 5$ % was favored for several reasons. First, lower relative densities of <6 % pertain to reinforced concrete civil infrastructure columns [67,68] which typically use volumetric reinforcement in the range of 3–5.5 % in the non-critical areas when the volume of both longitudinal and transverse reinforcement is considered in the volume of the element. Non-typical heavily reinforced cross-sections can achieve volumetric relative densities of 7% up to 9.5% [69]. Additionally, the manufacturing of IPCs and the satisfactory compaction of the soft matrix phase are only feasible on a millimeter scale with low relative density truss lattices. Thus, we investigate the enhancement of compressive properties with a small volumetric fraction of metal auxetic truss lattices added as a reinforcing and confining scheme.

To extract the elastic properties of a variety of different geometrical configurations of the selected architectures in order to determine the geometrical features that exhibit the largest increases of confinement pressure to the composite matrix, the bowtie and double pyramid unit cells were analyzed with the Abaqus/Standard (Dassault Systèmes) [70], using approximately 50,000–500,000 C3D10 tetrahedral elements with quadratic shape functions (element count being geometry dependent). Periodic boundary conditions were applied with the use of a Python script to eliminate edge effects. The nine elastic constants were calculated and obtained from the simulations using the procedure showcased by Yang and Becker [71] for orthotropic materials. The unit cell finite element computations were conducted under the assumption of small deformations and linear material behavior with material properties following the typical values of $E = 200$ GPa, $\nu = 0.3$ for the stainless steel bulk material.

Using the orthotropic elastic constants extracted from the unit cell models and $E = 4.4$ GPa, $\nu = 0.18$ for the concrete/mortar matrix phase, the Voigt model implemented by Tzortzinis et al. [37] was used to estimate the increase in confinement pressure $p^{(M)}$ acting in the matrix (Fig. 2) due to the passive resistance and lateral contraction of the auxetic truss. The matrix is assumed to be isotropic, with a reduction of the matrix stiffness due to the small volume occupied by the truss lattice calculated according to the Hashin–Shtrikman least upper bound [72]. Using this approach, the effective properties of the concrete/mortar region surrounding the truss regions is taken as $E = 3.98$ GPa, $\nu = 0.176$. Strain compatibility under axial compression is employed to split the loads between the two phases.

The explorative finite element investigation results illustrate the highest increase of confinement pressures in the lower range of transverse moduli, roughly from 300 to 2000 MPa (Fig. 2). A correlation between lower Poisson ratios and the increase in confinement pressure can be observed in the case of the two-angle double pyramid family of architectures, with the geometrical configurations achieving the largest increases in confinement pressures exhibiting the lowest Poisson's ratios for their respective transverse moduli. For the bowtie architectures, the highest increase in confinement pressures is achieved when $\theta < 80°$. However, it has been shown that architectures associated with lower θ angles achieve lower peak stresses when tested in axial compression outside of IPCs [17]. The relative increase in confinement pressures is also expected to shift slightly in case the elastic moduli of the two phases change. Six architectures were selected for the experimental study to harness the increase of confining pressure originating from highly compliant and lower Poisson ratio architectures. These architectures are the $\theta = 75°$, $\theta = 80°$, and $\theta = 85°$ for the one-angle, three-dimensional auxetic bowtie family and the $\theta_1 = 15°$ & $\theta_2 = 45°$, $\theta_1 = 15°$ & $\theta_2 = 60°$, and $\theta_1 = 30°$ & $\theta_2 = 48°$ for the two-angle double pyramid family. These architectural configurations represent increases of confining pressure > 20% and a wide variety of transverse and axial moduli while also providing directly comparable results to previous studies of bare truss lattices [17].

The elastic contrast between the composite matrix, which is assumed to have a Poisson's ratio of $\nu^M = 0.18$ from the literature, and reinforcing truss lattices allows the development of a mismatch transverse strain $\epsilon_m = \epsilon_t^{(T)} - \epsilon_t^{(M)}$ between the two constituents of the IPC. In the equation above, ϵ_m is the mismatch strain, $\epsilon_t^{(T)}$ is the transverse strain of the truss lattice, and $\epsilon_t^{(M)}$ is the transverse strain of the cementitious matrix. This mismatch of transverse strain generates an additional auxetic confining force on the IPC in the elastic regime and under the assumption of small deformations, where strain compatibility is enforced under the assumption that the two phases remain fully bonded. For the case of a convex honeycomb with $\theta = 100°$ bowtie, the elastic mismatch vanishes, and thus the auxetic confinement vanishes since $\nu^{(M)} = \nu^{(T)} \approx 0.18$, and similarly, for a convex unit cell or a non-auxetic reinforcing architecture of $\nu > 0.18$, strain compatibility is expected to reduce the confinement pressures acting upon the matrix.

3. Materials & methods

3.1. CAD modeling and manufacturing of stainless steel truss lattice specimens

To study the behavior of the selected truss lattice architectures in IPCs, modeling and manufacturing of finite-sized truss lattice architectures was performed. The finite-sized truss lattices were designed with tessellation sizes > 4 across every dimension to minimize the edge effects of the boundaries. The unit cell relative density was kept constant at $\rho^* = 5\%$, while the specimen dimensions were kept as close as possible to 2 × 2 × 2 in. to maintain close compatibility with

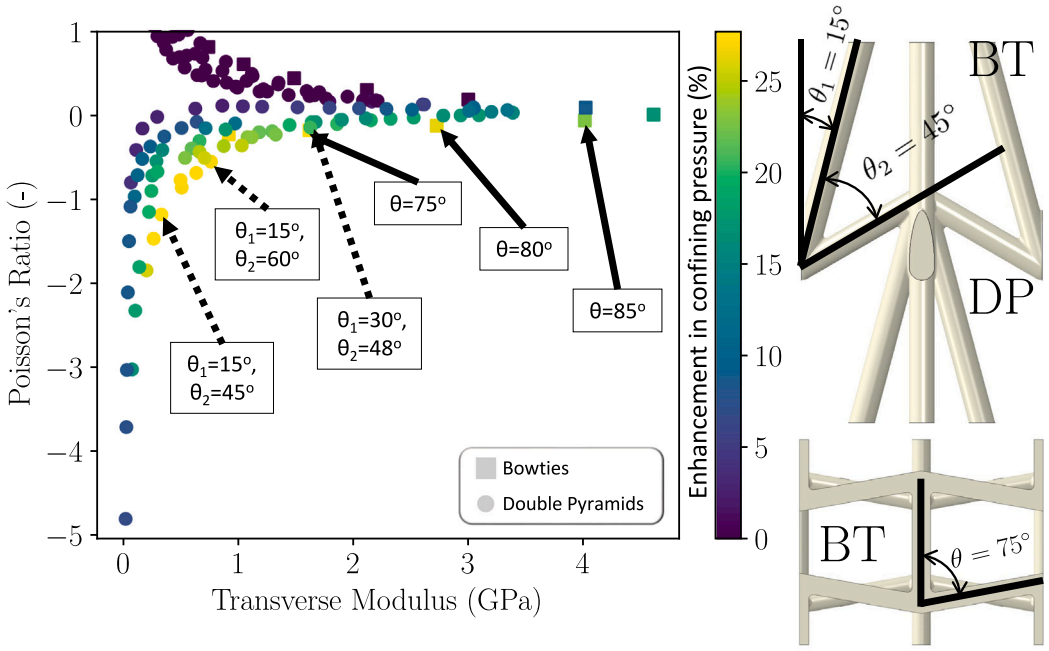

Fig. 2. Finite element results from a broad survey of bowtie and double pyramid architectures with different geometries. The unit cells of both the bowtie and double pyramid architectures were analyzed using periodic boundary conditions for a variety of characteristic angles (θ_1 and θ_2 for the double pyramids and θ for the bowties). The Poisson's ratio is plotted against the transverse modulus of the bare trusses. The confining pressure of the interpenetrating phase composites exhibits an increase near the lower boundaries of the data points presented, where the lower Poisson's ratios are achieved for each architecture.

the ASTM C109/C109M standard [73], which is utilized to measure the compressive properties of the cementitious matrix. The dimensions and specifics of each of the fabricated six architectures are presented in Fig. 3. The boundary edges of the specimens were designed and manufactured with full-diameter beams. A total of 18 truss lattices were manufactured for testing inside IPCs, with three repetitions out of each one of the six selected architectures. The procedure outlined by Vitalis et al. [17] was precisely followed using the same specimen dimensions, manufacturing methods, configuration, software resources, and equipment. The parametric design of the architectures took place in Rhino 7, with additional post-processing and preparation for additive manufacturing in Solidworks [74,75].

The laser powder bed fusion additive manufacturing method was selected for the fabrication of stainless steel truss lattices that exhibit adequately high elastic contrast with a cementitious matrix. For the fabrication of the specimens, a precipitation hardening 15–5 stainless steel pre-alloyed powder was used (EOS PH1), which exhibits excellent mechanical properties for general engineering applications. The stainless steel alloy was used in the EOS M290 selective laser melting metal 3D printer. The exposure settings used in manufacturing were derived from previous manufacturing studies [17]. For the infill, 320 W and a laser speed of 1300 mm/s were used, yielding a VED of 68.38 J/mm^3. Similarly, for the upskin 225 W and 841 mm/s were used, and for the downskin 315 W and 2700 mm/s, both yielding 74.32 J/mm^3 and 36.46 J/mm^3 accordingly. The selected layer recoating thickness for the process was 40 *um* and hatch distance was 0.09 mm. The specimens were removed from the manufacturing base plate with the use of a Wire EDM machine. No additional post-manufacturing treatment ensued, and the as-built truss lattices were embedded in interpenetrating phase composites right after manufacturing. The inherent surface roughness of as-built parts manufactured using laser powder bed fusion is desirable in IPCs due to its ability to enhance the bonding of the two phases, similar to the ribs and lugs present in conventional structural steel rebar.

3.2. Cementitious mortar matrix mix design

To study the improvement in the confinement in the case of auxetically reinforced IPCs, a cementitious mortar matrix was favored due to its superior mechanical properties compared to hydraulic lime or air lime mortars. It should be noted that conventional concrete structures are expected to achieve superior stiffnesses compared to sand–cement mortars [76]. Additionally, a lower effective stiffness of the reinforcing phase is expected, owing to the inherent anisotropy in the additive manufacturing of thin features with steep overhanging angles [17,77]. However, rapid prototyping using metal additive manufacturing and cementitious mortars can assist the study of the fundamental mechanics that arise in IPCs.

For determining the mix design composition of the cementitious mortars used for the composite matrix, an iterative approach was used to fabricate a finely tuned mortar with satisfactory flowability, which can effectively be compacted to avoid the presence of voids and gaps inside the matrix. The addition of a medium/high-range water-reducing agent was necessary to manufacture a mix that could flow inside every steel lattice. For that reason, the truss lattice prototypes were manufactured using polyamide 12 (nylon PA-12) in the EOS Formiga P110 Velocis to test a variety of mix designs and water-reducing agent variations (Step 1, Fig. 4). The molds used for casting the variable-sized truss lattices were manufactured using a commercial Ender S1 Plus FDM 3D printer and PLA filament, with extrusion temperature of 200 °C ± 1° and a glass build bed with a temperature of 60 °C ± 1°, with a 0.4 mm nozzle and layer thickness of 0.28 mm. The design of the molds is similar to the ASTM C109 2 in. molds with different dimensions from each other to accommodate the variable dimensions of the truss lattices with constant unit cell relative densities of $\rho^* = 5\%$. The wall thickness of the molds was designed to be approximately 0.84 mm, and a ~1 mm tolerance was left on every side to allow shrinkage.

The mortar's composition and mix procedure followed the ASTM standards and previous work as closely as possible [37,73,78]. The

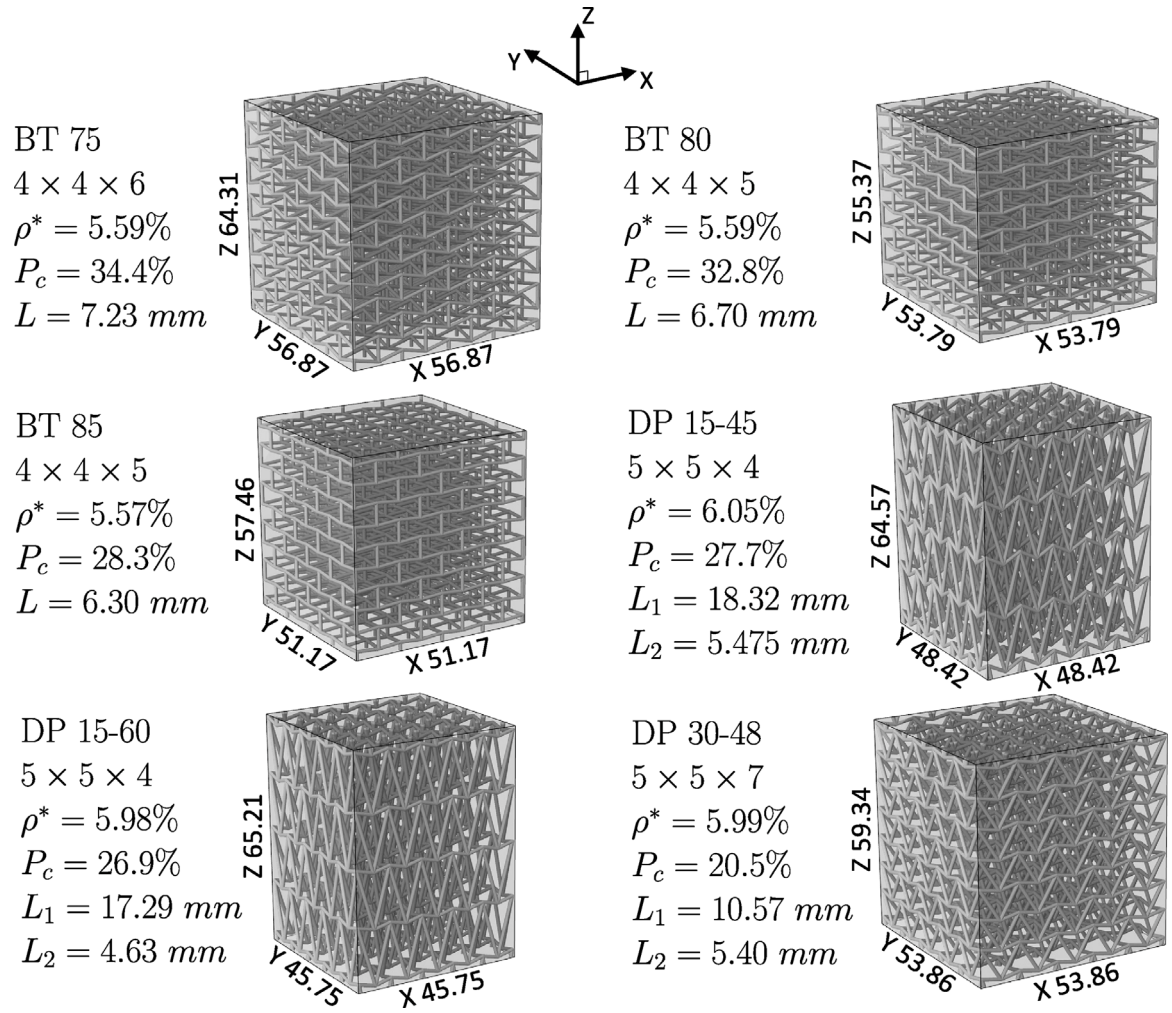

Fig. 3. Tessellations of the selected architectures with a constant periodic unit cell relative density of $\rho^*_{UC} = 5\%$, as designed in the CAD software. All unit cells are tetragonal. The as-built relative density slightly varies from 5% due to the different effects of the edge boundary conditions on every architecture. P_c indicates the relative percentage of increase in confining pressures from the exploratory finite element simulations for each one of the selected architectures (Fig. 2). The bowtie architectures maintain a constant strut length of L inside the tessellation, with their top & bottom boundary struts being $L/2$. The double pyramid architectures have struts of two different lengths: the long ones (L_1), which are inclined closer to the vertical Z direction, and the short ones (L_2), which are inclined closer to the XY plane.

Table 1
Mortar mix design based on modification of the ASTM C109/C109M, the standard test methods for the compressive test of hydraulic cement mortars. [73]. A slight increase in water-reducing agent was required to achieve satisfactory penetration of the mortar for every architecture compared to Tzortzinis et al. [37].

w/c ratio: 0.485	This work	ASTM C109/C109M
Fine sand (g)	1375	1375
Portland cement type I/II (g)	500	500
Water (mL)	220	242
Plastol 341s (mL)	33	–
Total batch (g)	2128	2117

batch size was kept at the proposed equivalent of six 2 in. specimen batch from the ASTM C109 to ensure adequate mixing and hydration of the mortar inside the 5-quart (4.73 L) mixing bucket. The mix design used finely graded pit sand ranging from 0.125–0.710 mm (with a SG_{dry} = 2.69 and water absorption=1.6% per ASTM C128-22 [79]) and Quickrete Type I/II portland cement (SG_{dry} = 2.6 – 3.15) [80]. The mortar compaction took place on a vibration table utilizing variable numbers of 60-second increments for each architecture (4 to 8 increments depending on the volume of the architecture) until every specimen was successfully compacted. The mortar was mixed using a handheld industrial mortar mixer, following the steps described in the ASTM C305 specification and approximately following the slow and medium speeds of 140 and 285 rpm [78]. The permeability of each specimen due to the differences in their architecture affected the difficulty of mortar compaction. Specimens with unit cells that avoided sharp re-entrant angles and were closer to forming cubic gaps were significantly easier to compact. The nylon specimens were left to cure for 24 h in their molds inside a saturated curing chamber at 75 ° F ± 2° and for another five days, saturated in water. On the 7th day, they were sectioned with a cutting wheel in three pieces each to ensure no large voids were present in the matrix (Steps 1 to 2, Fig. 4). Additionally, plain mortar specimens were tested under axial compression to ensure the mix design's compliance with the 10.9% deviation delineated by ASTM C109/C109M [73].

The final mortar mix design used for manufacturing the IPCs is presented in Table 1. After the determination of the mortar manufacturing protocol, the molding of the steel IPC specimens took place (Step 3, Fig. 4). The weight of each specimen was monitored to match or exceed the predicted weight needed to fill the matrix for each architecture. Multiple batches were cast using the same mortar protocol to prepare all 18 IPC specimens. The density of the plain mortar ASTM C109 2 in. cube was, on average, 2.34 g/cm^3 with a std. deviation of 0.031. Inside

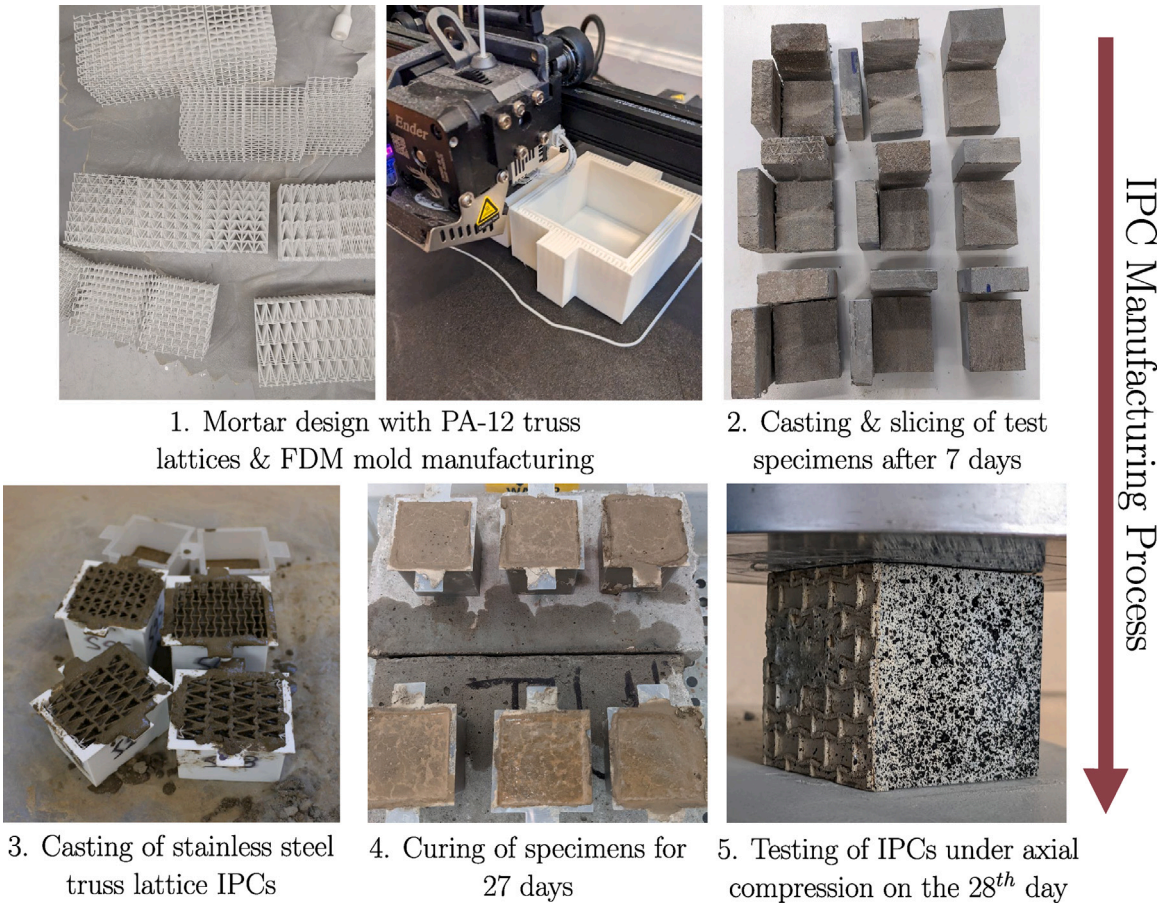

Fig. 4. Fabrication sequence for the mechanical testing of steel IPCs. 1. The mortar mix design is revised using nylon truss lattices to achieve satisfactory flowability and adequate penetration of the truss lattice specimens. Mold fused deposition modeling (FDM) manufacturing is commenced, and the molds are also tested with the nylon truss lattice composites. 2. Sectioning of the specimens verifies the absence of large macroscopic pores. 3. Once the mortar mix and design protocol are finalized, the steel truss lattice IPCs are cast. 4. The steel IPCs are cured in a temperature and humidity-controlled environment. 5. The IPCs are tested under axial compression after 28 days of curing (the rigid plates at the top and bottom are visible).

the steel-reinforced IPC specimens, the average mortar density was 2.41 g/cm^3 and the std. deviation was 0.052, which can be attributed to slightly higher compaction due to the vibration of the metal lattice in the matrix. The steel IPCs were cured for 24 h in their molds in a saturated curing chamber at 75 ° F ± 2° and were immersed in water after 24 h for 27 days (Step 4, Fig. 4). On the 28th day, the specimens were removed from the water, sanded to avoid edges that can cause strain concentrations, and tested in a saturated condition under axial compression (Step 5, Fig. 4). In addition to the composite IPCs, five 2 in. cubic ASTM-compliant plain mortar specimens were manufactured to study the properties of the cementitious mortar matrix present in the IPCs.

4. Experimental & computational results

4.1. Experimental testing of IPCs

For the quasi-static mechanical testing of the interpenetrating phase composites under monotonic axial compression, the same experimental setup as in the previous work by Tzortzinis et al. [37] was used. The specimens were tested monotonically under axial compression using a displacement-controlled method and ~1.0 mm/min displacement rate. Two Novotechnik 100 mm linear potentiometers with a 0.002 mm repeatability were mounted on a Forney 400 high-stiffness frame, with an Omega 2.5D through hole 100,000 lbf load cell placed under the plate to record the applied force. The measured displacement was the average of the two linear potentiometers. For the data acquisition, a DataQ Instruments DI-710 data logger was used along with a Vishay P3 strain indicator and recorder, both synchronized at a recording rate of 1 Hz per channel.

First, five unreinforced ASTM 2in. cementitious mortar specimens are tested to determine the mechanical properties of the matrix phase. The results of these experiments are later used as a probe into the statistical variability of the mortar between different batches and to calibrate the mortar material in computations (Fig. 5). Next, experiments of 18 IPC specimens in axial compression follow using the setup earlier described. Out of these specimens, 17 IPCs are tested in their primary testing direction Z (Figs. 3 and 6), while one is tested in the secondary X/Y direction to provide experimental evidence of the difference between the two (Fig. 8). During the testing procedure, images were taken at approximately 3 fps using a Canon 80D DSLR camera to document the experiment process and report findings of the apparent failure modalities of the composites (Fig. 7).

4.2. Results-discussion

The unconfined mortar specimens present a slight variability of peak stresses and strains (Fig. 5), which can be explained by the different batches that were cast using the same mix design (Table 1) to manufacture all the samples. This variability is also carried over to the results of the experimentally tested IPC specimens (Fig. 6). The effect is pronounced in the cases of the 85 bowtie and the 15–60 double pyramid architectures due to the presence of the lowest and highest matrix strengths in their batches, respectively. The inclusion of

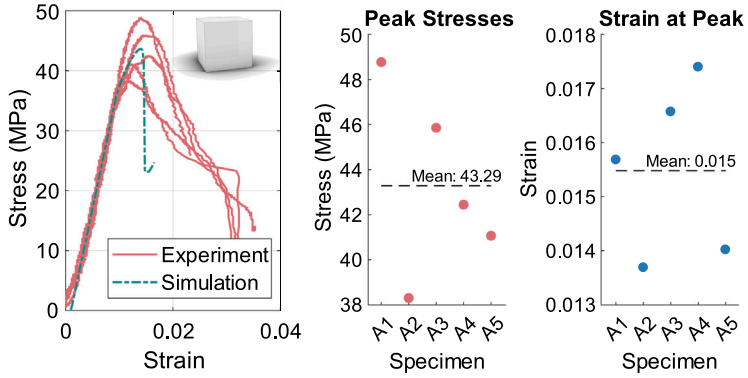

(a)

	Elastic Modulus (MPa)
Mean	4396
Median	4321
25^{th} Percentile	4225
75^{th} Percentile	4533
Min	4088
Max	4881
Std. Deviation	297

(b)

Fig. 5. (a). Stress–strain curve analysis for the five (A1–A5) unreinforced ASTM 2in. cementitious mortar cubes with siliceous pit clayish sand and a binder-to-aggregate ratio of 0.36. and (b). The measured elastic modulus metrics for the same set of specimens.

all specimens in one batch can reduce the in-batch variability of the mortars.

The results of the mechanical testing of the six IPC architectures under axial compression (Fig. 6) illustrate a remarkable increase in the peak stresses (from 175% for the 15–60 double pyramid to 378% for the 85-degree bowtie) and ductilities (in the range of 107% for the 15–60 double pyramid to 467% for the 80-degree bowtie) of the specimens for the auxetically confined schemes compared to the experimental results of the unconfined mortar specimens (Fig. 5). Four main mechanisms can describe the improvement in the mechanical response of the auxetically confined composites: 1. The combination of passive and auxetic confinement forces developing due to the strain mismatch of the two phases. This mismatch strain is expressed as $\epsilon_m = \epsilon_t^{(T)} - \epsilon_t^{(M)}$, and for sufficiently small loads in the elastic region, it generates the confining pressure P_c exerted by the struts of lattice to the surrounding mortar via the 45° angle arching stress mechanism described by Mander et al. [51]. Thus, the effectively confined matrix core is formed for each architecture. 2. A transition of the architectures from bending-dominated to stretching-dominated [82,83] due to the presence of the composite matrix is observed, limiting bending inside the trusses. Consequently, the reinforcing auxetic truss lattice phase inside the interpenetrating phase composite leads to increased hydrostatic compression of the matrix, 3. Additionally, the dense, thin struts that constitute the reinforcing phase of the IPC assist in crack bridging in a similar manner that is exhibited in fiber-reinforced concrete (FRC), thus stopping rapid crack propagation that would be exhibited in an unreinforced specimen [84]. This mechanism also affects the post-peak behavior and the ductility at the post-peak region [85]. Eventually, strut/matrix debonding takes place, followed by tensile failure of the debonded struts. The crack-bridging effect can be further studied by examining various tessellation sizes with similar relative densities ρ^*, which can be achieved via varying strut thicknesses t, to observe the crack-bridging behavior of various numbers of struts in a lattice under axial compression, 4. The additional strength and stiffness provided by the reinforcing phase itself can be tailored by altering the geometrical parameters and architecture of the reinforcement. The final mechanical properties of the composite rely on a combination of changes in the effective lateral pressure P_c acting upon the matrix (Fig. 3), the ultimate strength and the stiffness of the reinforcing phase [17], and the vertical spacing of the almost horizontal (laterally confining) struts, which produce arching confining stresses upon the matrix similar to those that are produced by conventional hoops [51].

The gain in terms of peak stresses and ductility due to the auxetic confining scheme is larger for all three bowtie architectures compared to the double pyramid architectures. Significant differences are also present in the deformation modes between the specimens (Fig. 7) . The bowtie architectures place their close-to-horizontal inclined struts under significant tension, which is observable with the lateral expansion of the specimen before the first load drop. Fracture initiation for the 75-degree bowtie is exhibited as a vertical tensile failure plane of a series of struts, followed by a progressive failure of nearby struts in an ‘unzipping’ manner. For the 80 and 85-degree bowtie, the same mechanism of tensile failure is observed. However, the failure planes are inclined in these two cases. Videos delineating the failure modes mentioned above have been included as supplementary information. The 15–45 and 15–60 double pyramid IPCs exhibit different failure modes due to the shape of their unit cells, facilitating a larger aspect ratio, which leads to larger distances between the lateral constraint struts, thus increasing unit cell slenderness (Fig. 3). The increased unit cell slenderness for these architectures leads to premature buckling of the exterior layer of struts (Fig. 7). Furthermore, the fewer close-to-horizontal struts present in those architectures provide fewer opportunities for the arching confinement stresses to transfer to the matrix effectively under 45° angles. In the case of the 15–45 double pyramid, a combined tensile and buckling failure is observed, while the 15–60 architecture illustrated buckling and collapse of the upper layers of unit cells without exhibiting a significant amount of tensile fractured struts. On the contrary, the 30–48 double pyramid architecture exhibited a failure mode similar to the bowties, with the tensile splitting of the struts in vertical failure planes being dominant. These findings present a pattern in which the two architectures with the highest transverse moduli (85 and 80-degree bowties) facilitated tensile failure modes with inclined failure surfaces, the architectures with intermediate transverse moduli (75-degree bowtie and the 30–48 double pyramid) exhibited tensile splitting fracture parallel to the testing axis failure planes and the most compliant architectures presenting a mix mode buckling failure. However, this does not necessarily imply direct causation since the failure modes are also heavily dependent on the unit cell shape and aspect ratio.

Despite the expected in-group variability, conclusions can be reached on the compressive performance for every architecture. The ultimate strains and elastic moduli present slight variations between the samples in a consistently narrow range of values, similar to the unconfined mortar specimens (Fig. 5). After casting the specimens, and only in the case of the bowtie 75, a ±1 mm deviation in the top surface height for two out of three specimens was observed, leaving the struts of the top surface partially exposed. This was due to the large volume of the specimen, leading to increased shrinkage during curing compared to the smaller specimens. These 75-degree specimens experienced somewhat reduced ductility despite reaching peak stresses similar to those of the third specimen (Fig. 6). The influence of boundary WEDM cuts could also affect the response of the IPCs, but in the absence of severe defects, the influence of support cutting is expected to be statistically insignificant. No significant defects were reported in any of the truss lattices tested in this work.

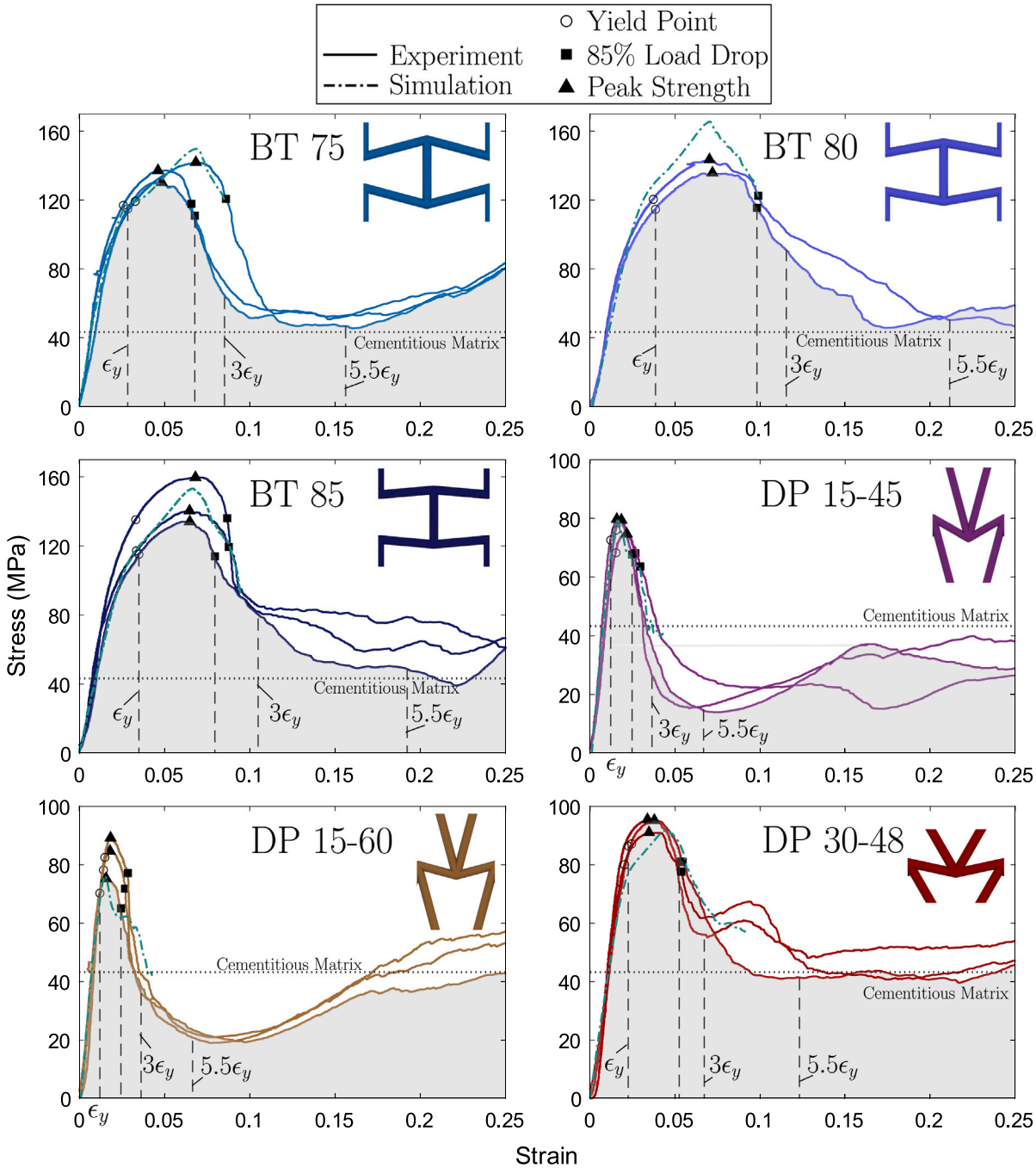

Fig. 6. Stress–strain curves of auxetic reinforced composite experiments and computational simulations for both bowtie and double pyramid architectures. The yield points are determined using the 3/4 method discussed in Section 4.5 [81]. The average peak stress of the unconfined mortar matrix is presented with a horizontal dotted line. A remarkable difference between achieved peak stresses is noticeable between the two architectures, with the bowties achieving significantly higher peak stresses and ductilities compared to the double pyramids. Both auxetic reinforcing schemes enhance the confinement of the mortar matrix, exhibiting a notable increase in the compressive properties compared to unconfined specimens (Fig. 5). Computational simulation results are presented using a constant matrix strength equal to the observed mean value of unreinforced matrix strengths (43.29 MPa).

In addition to the results of the bowtie architectures tested on their Z axis (Fig. 3), one of the 80-degree bowtie specimens, which was designed to be almost cubic, was tested rotated 90° to its side to compare the specimen's response in its weaker axis (Fig. 8). This experimental comparison was particularly interesting to observe potential variations in the mechanical behavior on the specimen in different axes, since the bowtie architectures are auxetic in both orientations, contrary to the double pyramid architectures. An initial softening was observed for the specimen tested on the X/Y orientation, which can be attributed to cracking/crushing of thin mortar layers at the top/bottom perimeters until contact of the metal truss lattice with the compressive platens is fully developed. A 24.7% decrease in the peak stresses was observed when the specimen was tested on its weak orientation X/Y, with no significant alterations in its stiffness or post-peak behavior when

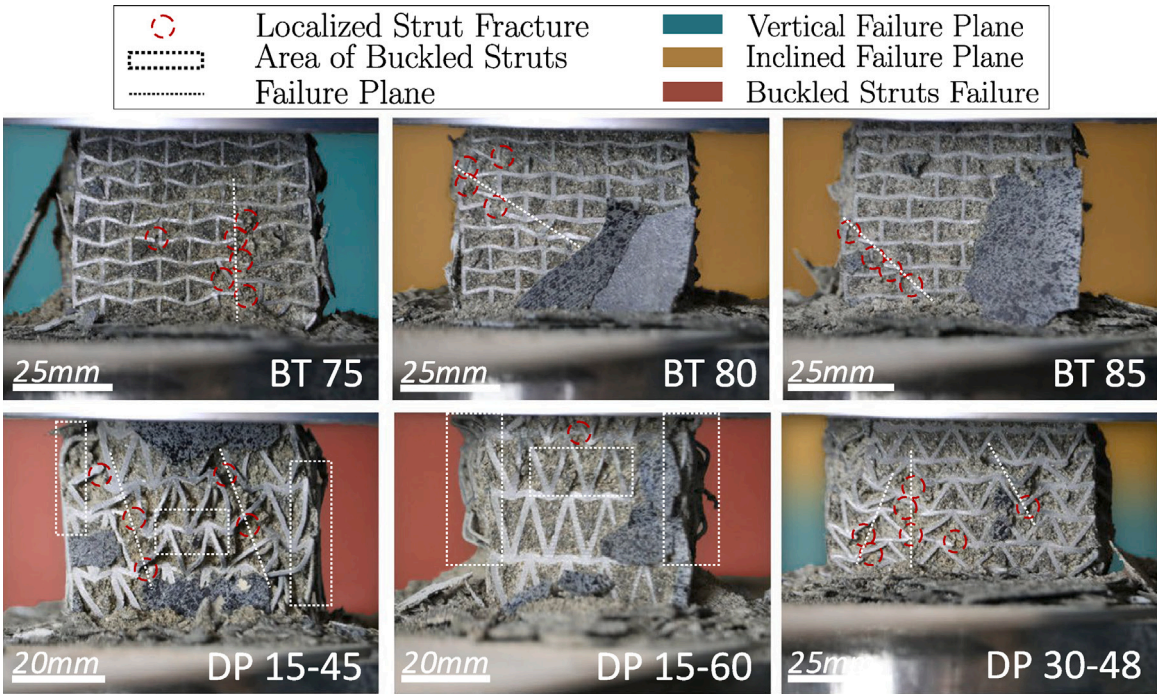

Fig. 7. Images taken in the post-peak region of all the experimentally tested auxetically reinforced composites. Failure modalities are categorized by background color. Blue indicates vertical failure planes, yellow indicates inclined failure planes, and red indicates areas of buckled external struts. The images were taken after the collapse of the thin exterior layer of mortar between the boundaries of the truss lattice and the mold. (For interpretation of the references to color in this figure legend, the reader is referred to the web version of this article.)

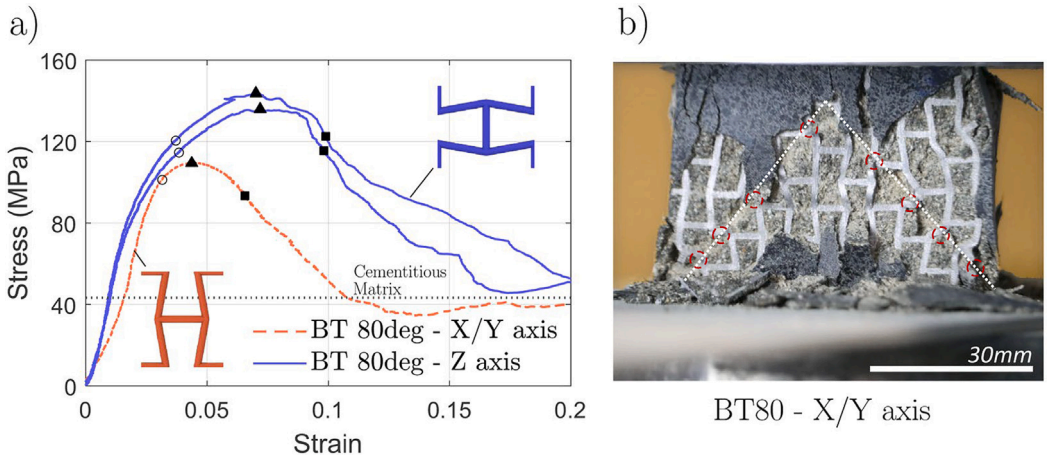

Fig. 8. (a) Stress–strain curves of two testing orientations of the 80-degree bowtie specimen. The primary testing orientation (strong orientation) studied in this paper illustrates a 27.5% average increase in the peak strength of the specimen when compared to the alternative 90° orientation without significant alterations in the stiffness or post-peak ductility of the specimen. A similar response is expected from other bowtie architectures. (b) The failure mode of the 80-degree bowtie at large strains in the post-peak region. Two inclined failure planes can be observed, leading to the splitting of the composite.

compared to its counterparts tested in the primary Z-axis direction. This proved further that the optimal orientation was selected during the experimental study of the bowtie IPCs.

4.3. Computational validation of experiments

A finite element analysis of the mechanical models was performed using Abaqus/Explicit [70] to validate the experimental results. The modeling approach remained the same for all the finite-sized simulations performed. The auxetic truss lattice is meshed using C3D4 tetrahedral elements, and the mortar matrix is simulated using C3D8R hexahedron brick elements with reduced integration. The mesh properties of each computational model can be found in Table 2. The approximate element size remained the same for each model, and the resulting number of elements varied according to the composite's spatial complexity and physical dimensions. The composite behavior was modeled by defining an embedded region constraint between the cuboid matrix (host elements) and the solid truss lattice (embedded elements). Equivalent material models were developed based on experimental data, including build-angle anisotropy effects. The elastic moduli used were 4396 MPa (mean of measurements) for mortar (Fig. 5), 140 GPa for the bowtie architectures, and 75 GPa for the double pyramid architectures considering the anisotropy of inclined printed thin members induced by the LPBF manufacturing process [17]. To model the plastic properties of the mortar, a concrete damage plasticity model was employed using a dilation angle $\theta_{dil} = 40°$, eccentricity of 0.1, $f_{b0}/f_{c0} = 1.16$ and $K = 0.666$. The inelastic properties

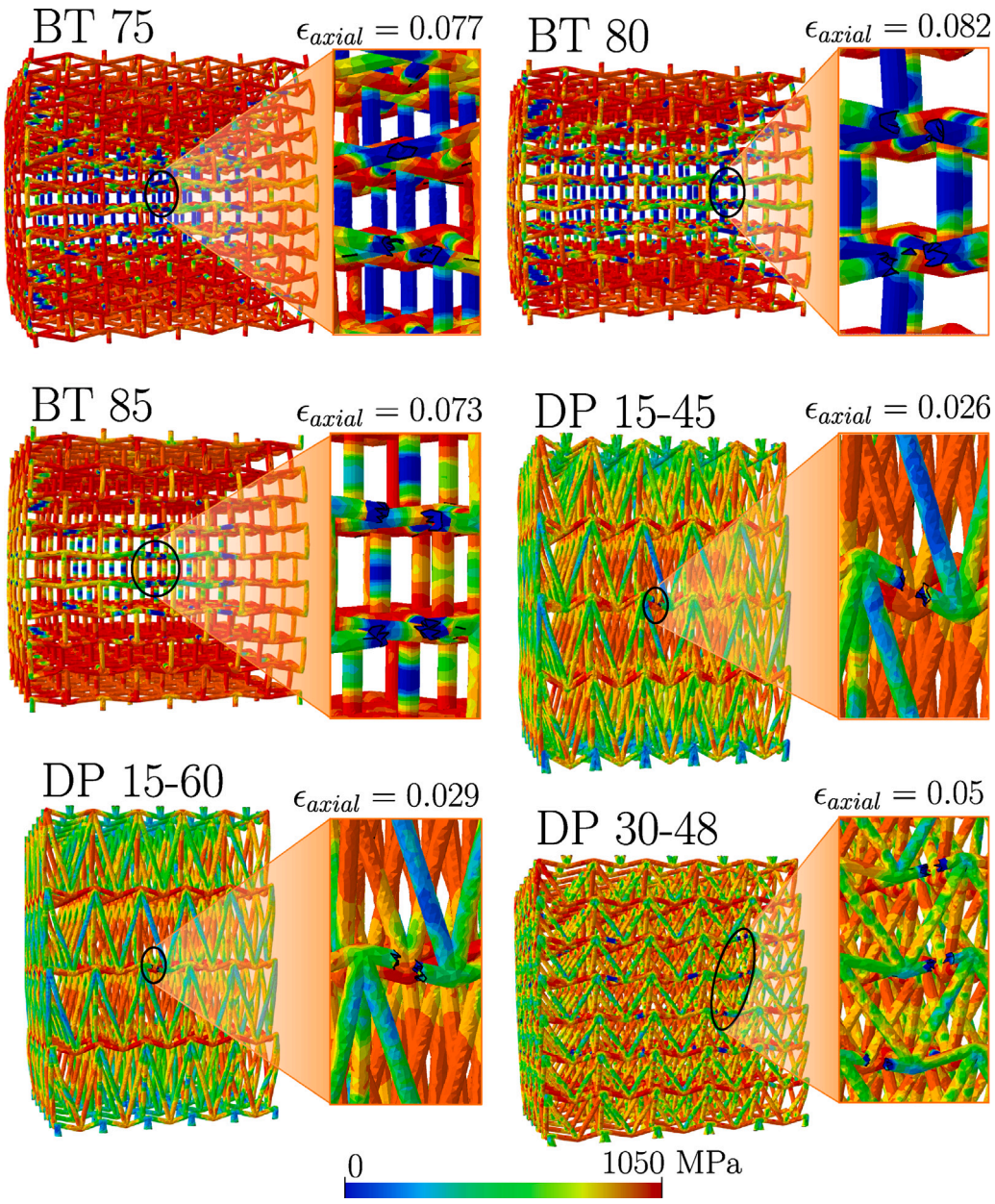

Fig. 9. Von-Mises stresses contour maps isolating the truss lattices in the composites and delineating the locations of the first fractured element in each composite architecture from the finite-sized simulations. For every architecture, fracture initiates on the free surface of the truss lattice on diagonally inclined struts close to the horizontal direction. The figure presents contour maps right after the peak stress location for each architecture. Significant differences between the stress distributions can be observed between the two architectures, with the bowties reaching higher hydrostatic stresses, leading to increased load-bearing capacities. The dark blue areas indicate elements that have exceeded their peak strength in the plastic region and are experiencing softening before fracture . (For interpretation of the references to color in this figure legend, the reader is referred to the web version of this article.)

in compression were derived from the mean measured experimental values with a peak at 43.29 MPa, while the tensile properties were ~10% of the compressive values. The effective plastic law of the steel truss was defined as 850 MPa at first yield (0 plastic strain), 1050 MPa at 0.06 plastic strain, 850 MPa at 0.085 plastic strain, and 1 MPa at 0.135 plastic strain (ϵ_{pl}), which approximates the loss of load carrying capability due to fracture. A ductile damage material model was also employed to alleviate convergence issues related to strain softening behavior of the plastic flow curve. The strain to failure for truss lattices in the IPCs was set to 0.14 of total strain ($\epsilon_{tot} = \epsilon_{el} + \epsilon_{pl}$) for a stress triaxiality of 0.33. The finite element mesh is not sufficiently refined to resolve the large strain and triaxiality gradients that exist just prior to fracture, therefore these values are interpreted as averages over comparatively large volumes of materials in a manner that is consistent with the mean fracture strain from the powder specification and the experimentally attained material testing data for inclined thin strut features in tension [17]. Element removal due to ductile damage took place at displacements at failure that yielded 0.18 of total strain. Constant displacement was applied monotonically using analytical rigid plates with a friction coefficient of $\mu = 0.2$ to model the tangential behavior between the steel base plate and cementitious sand mortar [86]. Computations were run up to displacement a little past the peak since the assumption of fully bonded phases stops being realistic for fully fractured cross-sections. In the experiments, this is observed with the collapse of the outside layers of struts shortly before the peak region and the separation of the struts from the matrix in the post-peak regime (e.g., buckled struts). Specifically, the maximum applied

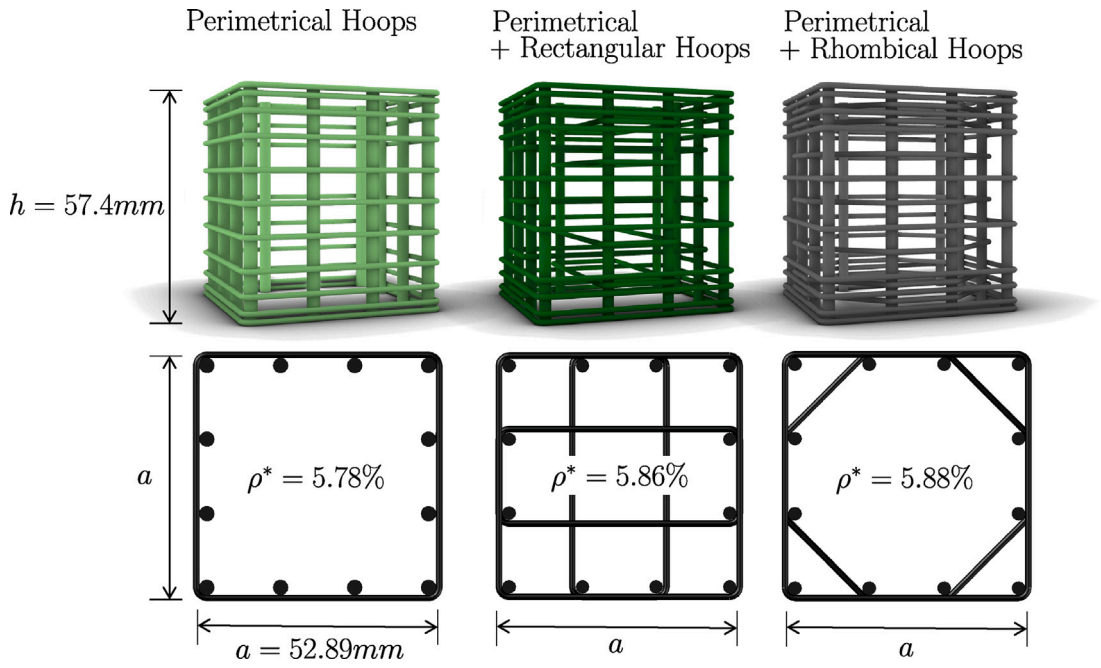

Fig. 10. Schematic of conventional reinforced concrete column detailing. The presented designs were constructed with similar relative densities ρ^* and dimensions to the ones of the experimentally tested auxetic specimens (Fig. 3) and were simulated to assess and compare the performance of each confinement scheme, using the same computational parameters that were used for simulating the IPCs as a baseline.

Table 2
Finite element computation mesh properties. The mesh dimensions are shown for the tetrahedral and hexahedral elements used for the truss and matrix. The average element size used was similar between the analyses. The resulting element number differed based on the spatial complexity of each structure.

	Truss (C3D4)		Matrix (C3D8R)		DOFs
	Tet Size	Element #	Hex Size	Element #	
BT 75 (4 × 4 × 6)		22.21E+5		198E+3	243E+4
BT 80 (4 × 4 × 5)		24.00E+5		202E+3	248E+4
BT 85 (4 × 4 × 5)		21.12E+5		212E+3	230E+4
DP 15-45 (5 × 5 × 4)		21.36E+5		210E+3	232E+4
DP 15-60 (5 × 5 × 4)	0.4 mm	20.60E+5	0.9 mm	195E+3	221E+4
DP 30-48 (5 × 5 × 7)		23.60E+5		222E+3	253E+4
Conv		9.50E+5		212E+3	147E+4
Conv-Rect		15.40E+5		212E+3	195E+4
Conv-Rhomb		9.80E+5		212E+3	149E+4

Table 3
Drawing details of the three conventional column confinement schemes to achieve relative densities close to the relative densities of the IPCs (5.59-6.05%, Fig. 10). The first three hoops are placed with spacing of s = 2 mm/4 mm/4 mm from each other to ensure failure in the middle of the specimens.

	Perimetrical hoops	Perimetrical + Rectangular hoops	Perimetrical + Rhombical hoops
Longitudinal rebar spacing (mm)	16	16	16
Transverse rebar spacing (mm)	6	6	6
Longitudinal rebar diameter (mm)	1.65	1.4	1.45
Transverse rebar diameter (mm)	0.7	0.7	0.7

compressive displacements are 5.5 mm for the bowties and the 30–48 double pyramid and 2.75 mm for the other two double pyramids.

The computational results present good agreement with the experiments of every architecture (Fig. 6), given the range of mechanical characteristics each individual specimen's matrix exhibits. Agreement between the typicalities of the failure modes in both experiments and simulations is also observed. For the case of the 80-degree bowtie and, to a lesser extent, for the 75-degree bowtie, the finite element analysis suggests that the cementitious matrix of the experiment has lower strength than the average properties used in the simulations. Such variance is expected since ±12.7% uncertainty was observed in matrix measurements. For all other specimens, the predicted peak strength is in close range of experimentally tested results.

Utilizing the finite element analysis results, the localized failure initiation of each truss lattice has been characterized and described (Fig. 9). The first fracture is always concentrated on the horizontal elements on one of the free surfaces of each specimen, with damage propagating through the nearby horizontal struts of the first fractured element. The Von-Mises stresses contour maps of the bowtie architectures indicate much higher peak stresses and strains throughout the architecture when compared to the double pyramids. Therefore, the spatial arrangement of the bowtie architecture is significantly more efficient at dissipating energy and uniformly distributing the stresses inside the lattice before failure, achieving a closer-to-hydrostatic stress distribution.

4.4. Comparison with conventional confinement schemes

Three conventional column confinement detailings were designed to produce comparable specimens to the auxetic truss lattices to further compare the auxetic confinement scheme with traditional confinement schemes used in the reinforced concrete construction practice. The relative density and specimen dimensions of these specimens (shown in Table 3 and Fig. 10) were designed to resemble the auxetic truss lattice specimens. Rebar diameters and spacing were designed to achieve a pragmatic design that maintains a transverse-to-longitudinal diameter ratio of 1:2, combined with achieving relative density constraints and spacing that was denser near the ends to avoid localized end failures. Well-studied confinement configurations from the literature inspired the designs [48,49,52,67,87]. Computational models were developed, utilizing these architectures in composite cuboid sections, to determine their effectiveness in confining concrete. These models used the same definitions presented in the previous finite-sized IPC computational

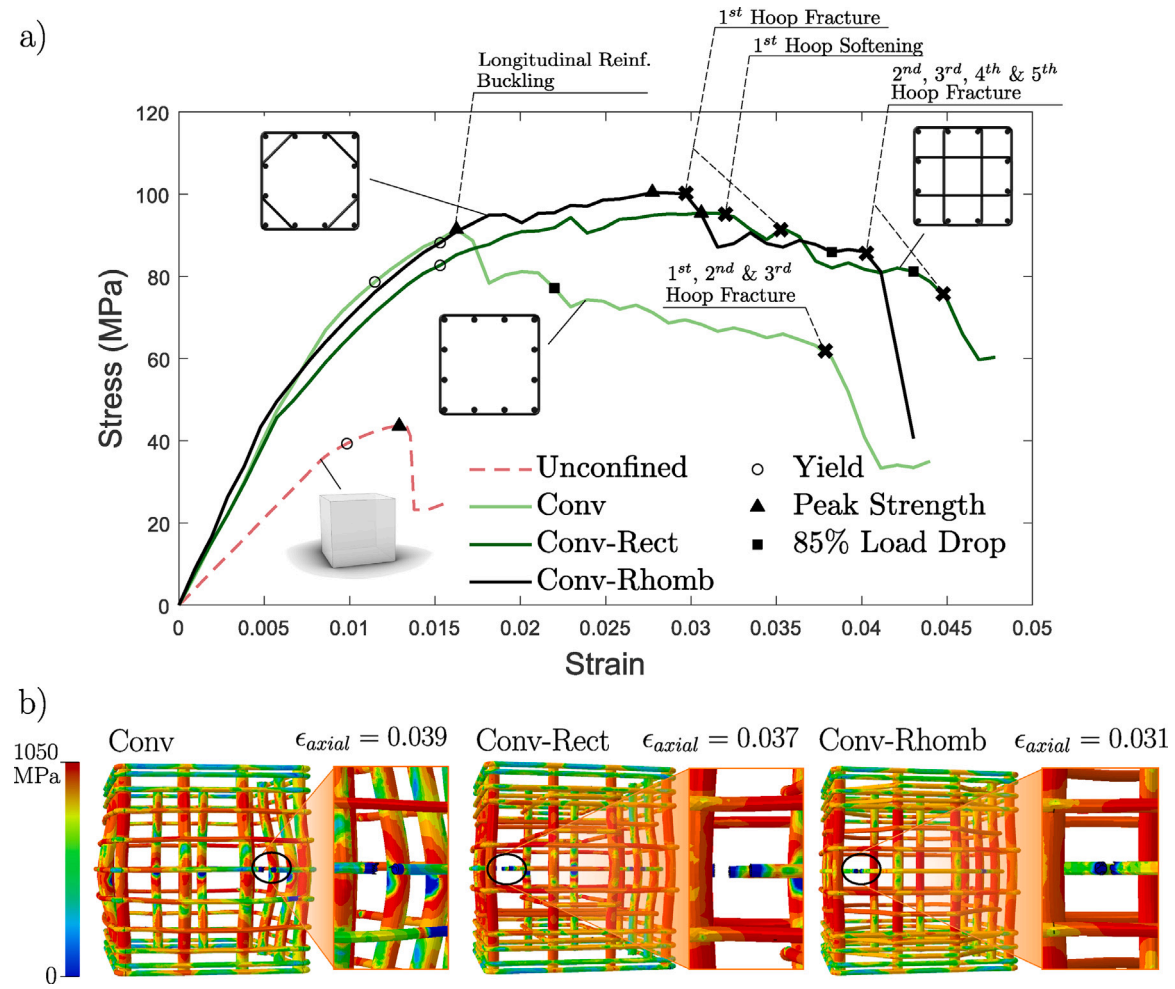

Fig. 11. (a) Stress–strain curves of simulated conventional reinforcing schemes (Fig. 10 and Table 3), with the failure progression being delineated. All conventional architectures exhibit rapid hoop fracture and strength loss after the fracture of the first hoop. (b) Von-Mises stresses contour maps isolating the conventional composite steel detailing and presenting the locations of the first fractured element in each composite architecture from the finite-sized simulations. For every design, fracture initiates after buckling of the longitudinal reinforcement and localizes in the lateral hoops, confining the middle part of the column.

models, which were successfully used to validate the experimental results for the entire range of IPC architectures. The elastic moduli used for simulating the conventional architectures was the typical 200 GPa used for reinforcing steel rather than a reduced value caused by laser powder bed fusion-induced anisotropy. The transverse and longitudinal reinforcement was designed to be monocoque, assuming adequate tying of the lateral hoops and fracture due to yielding instead of slippage.

All three conventional confinement schemes exhibit the same expected failure mode [48,52,67]. The compressive failure of the column is initiated with the yielding of the longitudinal reinforcement bars, followed by the buckling of the yielded longitudinal reinforcement combined with the expansion of the effectively confined matrix core. This leads to the rapid increase of stresses of the lateral confining hoops in the center of the column. Eventually, yielding and fracture of the central hoops ensues, and progressively, stress redistribution leads to fracture of the neighboring hoops, leading to the compressive failure of the column (Fig. 11).

The computational comparison of the auxetically reinforced specimens with the conventional confinement schemes illustrates a clear superiority of the bowtie-confined specimens in terms of peak stress and ductility (Fig. 12). All bowtie IPCs exhibit similar peak strains and slightly varying peak stresses. On the other hand, the double pyramid architectures exhibit slightly worse mechanical characteristics than the conventional reinforcement strategies for the two architectures (15–45 and 15–60 double pyramids) with buckling-dominated failure modes. Interestingly, the 30–48 double pyramid architecture exhibits a much more ductile failure than any other conventional or double pyramid design. This could be attributed to the tensile splitting failure mechanism that is activated in the 30–48 double pyramid, while all other aforementioned architectures experience buckling-induced failures.

In terms of stiffness, the 80, 85-degree bowtie, and the 30–48 double pyramid present stiffnesses statistically similar to the unconfined specimen (94% to 106%), while the 75-degree bowtie, the 15–45, and 15–60 double pyramid architectures illustrate higher axial moduli (in the range of 139% to 163%). All conventional architectures present significantly higher axial moduli due to a larger volumetric proportion of their reinforcement contributing to carrying the axial load. A non-rule-of-mixtures behavior is observed both in terms of the observed stiffnesses and peak stresses for the auxetically reinforced specimens — the architectures that demonstrate the highest stiffnesses and peak stresses as bare trusses [17] do not achieve the highest stiffnesses and peak stresses when embedded in mortar. This behavior is a consequence of the transition of the IPCs from a bending-dominated to a stretching-dominated response [37].

An investigation of the effective Poisson's ratio for the IPCs in the early stages of loading has revealed a reduction in most specimens' Poisson's ratio due to the presence of auxetic and conventional reinforcement strategies compared to the unconfined specimens (Fig. 13). While this reduction does not strictly correlate with the observed enhancement percentages of the mechanical properties, specimens that exhibit the largest enhancement also exhibit the largest

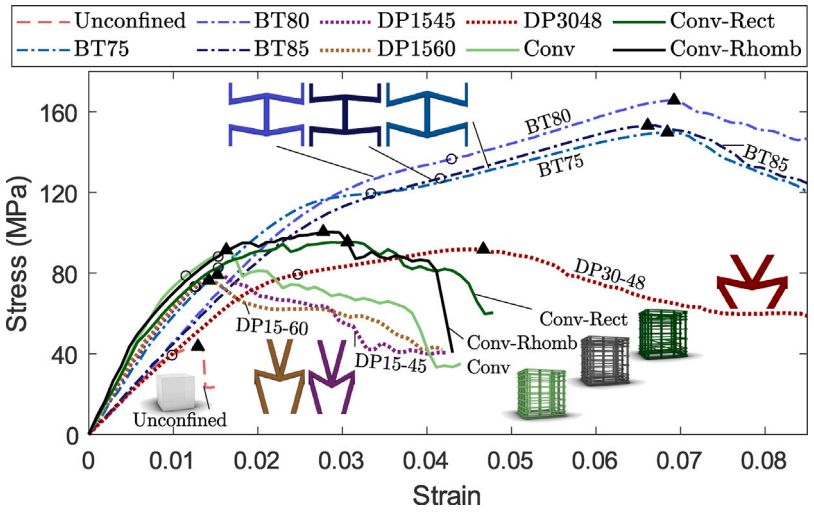

Fig. 12. Stress–strain curves of all computations run with a mean peak mortar strength of 43.3 MPa to isolate the effect of mortar variability within different batches. Results for the conventional architectures are presented with solid lines, and compared to the auxetic reinforcement scheme. All reinforcing architectures achieve significant improvement in the compressive properties of the composite. The double pyramid architectures achieve a similar increase of the peak loads as the conventional reinforcing scheme. The bowtie architectures present much higher peak stresses and strains, with large work dissipation in the elastic and plastic regions.

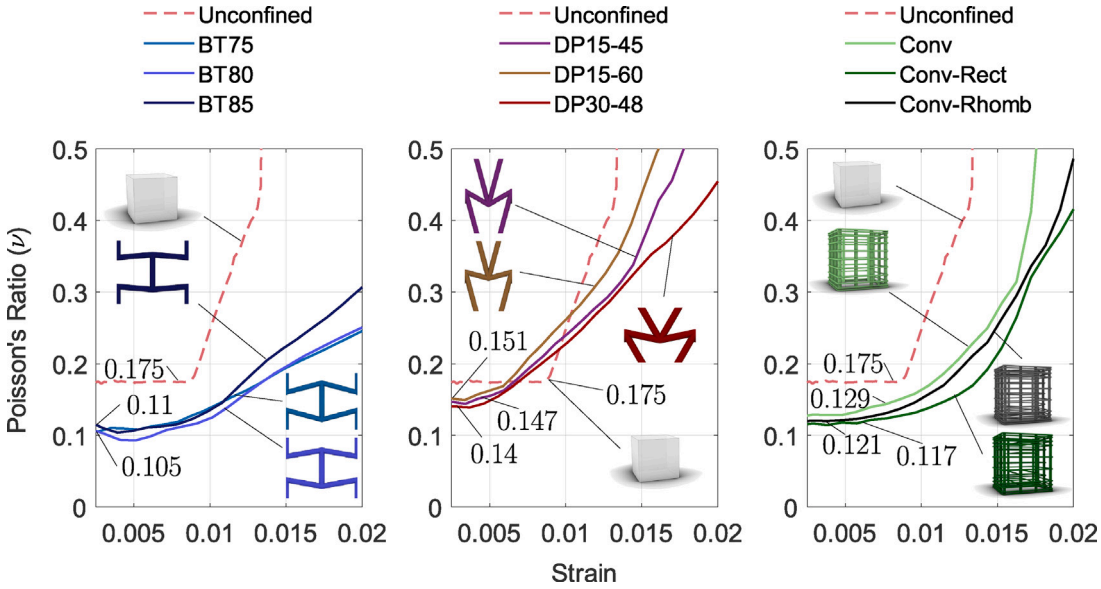

Fig. 13. Poisson's ratios ν progression at the elastic region and yield for the unconfined, auxetically, and conventionally confined specimens. The presence of reinforcement remarkably affects the effective Poisson ratio of the composite section, with architectures that initially exhibit lower Poisson ratios generally achieving higher peak loads and higher ductilities. The bowtie architectures present a better non-linear response compared to the double pyramids, which quickly, after 0.005 of strain, enter the non-linear region.

decrease in their effective IPC Poisson's ratio. Specifically, the 75-degree and 80-degree bowties exhibit the lowest Poisson's ratio at the beginning of loading, followed by the 85-degree bowtie and 30–48 double pyramid architectures. Higher values of Poisson's ratios are exhibited from architectures with buckling-dominated failure modes, such as the conventional and the 15–45 and 15–60 architectures. The unconfined specimens present a constant Poisson's ratio up to their yielding point (0.0085 strain), while the composite and reinforced specimens present an increasing Poisson's ratio due to the presence of geometric non-linearities within the reinforcement during strain progression. A decrease in the Poisson's ratio of the conventionally confined columns is also observed, with a distinct elastic range of up to 0.005 of strain. Overall, when looking at the ratio at different strain progressions, the composite specimens' Poisson's ratios can serve as a proxy that indicates stress states that mitigate the failure of the matrix via employing the mechanisms mentioned in Section 4.1.

4.5. Ductility

To assess the ductility of the experimentally confined members, the method proposed by Foster and Attard [81] was used to calculate the ductility indices D_c, I_5&I_{10}. To calculate the ductility indices, the yield strain is determined using the 3/4 method. Then, the combined ductility ratio D_c is derived from the division of the strain at which 85% of the peak strength is reached in the post-peak region, with the yield strain Eq. (1). The combined ductility ratio assists in assessing the near-peak ductility capacity of the structural member. Furthermore, the energy ductilities I_5 and I_{10} are evaluated by the division of the area A under the force-strain curve at the point of $3\times\epsilon_y$ divided by the area under

Table 4
Combined and energy ductility indices of the experimentally tested bowtie and double pyramid architectures, along with the computationally evaluated indices of the conventional reinforcing schemes. Values averaged from measurements within an auxetic specimen group (2 or 3 samples).

	D_c	I_5	I_{10}
BT 75 (4 × 4 × 6)	2.52	5.00	7.52
BT 80 (4 × 4 × 5)	2.61	4.99	7.44
BT 85 (4 × 4 × 5)	2.50	5.08	7.88
DP 15-45 (5 × 5 × 4)	1.90	4.64	6.43
DP 15-60 (5 × 5 × 4)	1.93	5.14	7.46
DP 30-48 (5 × 5 × 7)	2.40	5.82	9.82
Conv	1.98	1.51	1.78
Conv-Rect	2.18	2.44	2.82
Conv-Rhomb	2.34	1.86	2.13

the curve up to ϵ_y for the case of I_5, and the area of 5.5×ϵ_y divided by the area under the curve up to ϵ_y for the case of I_{10} Eqs. (2) and (3). This definition of the ductility index used in the determination of the energy ductility metrics is based on the plot area under the axial load N versus the axial strain ϵ_{axial}, thus allowing the consideration of residual capacity in the post-peak region. All three metrics numerically quantify the ductility of each composite architecture up to increasing strains while being strength agnostic.

The D_c value represents the metric of interest for civil infrastructure applications, representing the short-term ductility from yield to 85% load drop. The 80-degree bowtie architecture is superior in this area, followed by the rest of the bowtie architectures and marginally by the 30–48 double pyramid (Table 4). Considering the achieved peak stresses, the three bowtie architectures also generally illustrate significantly better mechanical properties than the double pyramids. The I_5 and I_{10} values correspond to the energy absorption in the post-peak compared to the 3/4 method yield point. In this domain, only the 30–48 double pyramid stands out due to its flatter residual capacity response in the post-peak, which is characterized by a milder drop from the peak load. Although the 30–48 double pyramid demonstrates remarkable energy ductility, it significantly compromises peak stress performance compared to its bowtie counterparts.

$$D_c = \frac{\epsilon_{0.85}}{\epsilon_y} \tag{1}$$

$$I_5 = \frac{A_{3y}}{A_y} \tag{2}$$

$$I_{10} = \frac{A_{5.5y}}{A_y} \tag{3}$$

The combined and energy ductility indices of the conventional reinforcing schemes were calculated from the computational models. The combined ductility indices D_c of the conventional are better than the 15–45 and 15–60 double pyramid architectures but fall short of every other auxetic architecture. The energy ductility indices I_5, I_{10} of the conventional reinforcing schemes demonstrate a less efficient ductile response of these reinforcing techniques, mainly due to the rapid loss of load-bearing capability after the first hoop fracture. The more efficient stress distribution inside the bowtie auxetic IPCs and the increased redundancy inherent to its design dramatically increase the combined and post-peak energy ductility of these architectures.

5. Conclusions

In this paper, we report results on the compressive properties of interpenetrating phase composites utilizing auxetic truss lattices to enhance the confinement of brittle mortar matrices. We have experimentally, analytically, and computationally studied the effect of three designs from two architecture families on the confinement of cementitious mortar composites under axial compression to identify how the auxetic actuation in an IPC can generate additional confining pressures that will improve the peak stresses and ductilities that can be achieved.

The key findings of this work are summarized below.

- All auxetic bowtie architectures exhibit significant increases in the peak strength and ductility of the IPCs. While the auxetic double pyramid architectures also boost the peak strength and ductility of the brittle matrix, their enhancement in IPC properties is much less pronounced. Overall, the auxetic reinforcing scheme succeeds in enhancing the confinement pressures for the brittle matrices using the bowtie architectures and increases the peak strength of the architectures by at least 165% and the peak ductility by 240% compared to the conventional column reinforcement strategies, using the most ductile 80-degree architecture and providing similar increases for the rest of the bowties. While tuning the characteristic angles of each architecture affects the IPC's post-peak response in axial compression, the influence on the peak stresses is less dramatic.
- Comparison of the auxetic bowtie reinforcing schemes to the conventional column reinforcing strategies has revealed a notable improvement in terms of achieved peak stresses and peak strains for all bowtie architectures. The 30–48 double pyramid, exhibits a significantly more ductile failure and post-peak response. The bowtie architectures can be considered good candidate unit cells for designing columns and beams for civil infrastructure that achieve superior mechanical properties. Upscaling advanced manufacturing techniques and robotic manufacturing can assist in adopting architected material-inspired reinforcing schemes on a real-life construction scale.
- A variety of geometrical configurations can produce specimens that achieve a high relative increase in the confining pressures of the IPCs. The increase in the confining pressure predicted by the calculation of the compliance tensors from the finite element analysis and a Voigt model assisted in finding architectures that increase the confining pressures up to 34.4%. The final compressive response of an IPC is dependent on a combination of mechanical properties, such as the axial modulus, transverse modulus, and Poisson's ratio, as well as on topological characteristics, such as the unit cell repetition pattern and the unit cell aspect ratio.
- The enhancement in mechanical properties directly translated into a reduction of the effective IPCs Poisson's ratio in the elastic region. The best-performing architectures exhibit the lowest IPC Poisson's ratio and a slower rate of Poisson's ratio increase over strain progression. Further study of this finding could assist in utilizing non-destructive methods by testing the elastic region to assess the IPCs' capacity and ductility.
- Calculation of the ductility indices for all auxetically reinforced specimens has shown remarkably increased combined and energy ductility indices, particularly for the three bowtie IPCs, and only a significant increase of the energy ductility indices for the double pyramid IPCs. This enhancement of ductile behavior present in the bowties can significantly benefit civil infrastructure applications due to the high combined ductility index and energy absorption applications due to the high I_5 and I_{10} indexes observed.

CRediT authorship contribution statement

Thomas Vitalis: Resources, Methodology, Investigation, Formal analysis, Data curation, Conceptualization. **Andrew Gross:** Writing – review & editing, Resources, Formal analysis. **George Tzortzinis:** Methodology, Investigation. **Brian Schagen:** Investigation. **Simos Gerasimidis:** Supervision, Resources, Project administration, Funding acquisition, Conceptualization.

Declaration of competing interest

The authors declare the following financial interests/personal relationships which may be considered as potential competing interests: Gerasimidis Simos reports financial support was provided by National Science Foundation. If there are other authors, they declare that they have no known competing financial interests or personal relationships that could have appeared to influence the work reported in this paper.

Acknowledgments

S. Gerasimidis would like to acknowledge the financial support of the National Science Foundation, USA (NSF CAREER Grant No. 2044705). The authors would also like to thank Mr. Dave Follette for his help with manufacturing the truss lattice specimens and Mr. Mark Gauthier for his extensive assistance with laboratory work.

Appendix A. Supplementary data

Supplementary material related to this article can be found online at https://doi.org/10.1016/j.conbuildmat.2024.139165.

Data availability

Data will be made available on request.

References

[1] Z. Wang, C. Jiang, P. Liu, W. Yang, Y. Zhao, M.F. Horstemeyer, L.-Q. Chen, Z. Hu, L. Chen, Uncertainty quantification and reduction in metal additive manufacturing, npj Comput. Mater 6 (1) (2020) 175, http://dx.doi.org/10.1038/s41524-020-00444-x, URL https://www.nature.com/articles/s41524-020-00444-x.

[2] Y. Xiong, Y. Tang, Q. Zhou, Y. Ma, D.W. Rosen, Intelligent additive manufacturing and design: state of the art and future perspectives, Addit. Manuf. 59 (2022) 103139, http://dx.doi.org/10.1016/j.addma.2022.103139, URL https://linkinghub.elsevier.com/retrieve/pii/S2214860422005280.

[3] M. Leary, L. Merli, F. Torti, M. Mazur, M. Brandt, Optimal topology for additive manufacture: A method for enabling additive manufacture of support-free optimal structures, Mater. Des. 63 (2014) 678–690, http://dx.doi.org/10.1016/j.matdes.2014.06.015, URL https://linkinghub.elsevier.com/retrieve/pii/S0261306914004646.

[4] G. Miao, W. Du, Z. Pei, C. Ma, A literature review on powder spreading in additive manufacturing, Addit. Manuf. 58 (2022) 103029, http://dx.doi.org/10.1016/j.addma.2022.103029, URL https://linkinghub.elsevier.com/retrieve/pii/S2214860422004213.

[5] B. Xiao, C. Chen, X. Yin, Recent advancements of robotics in construction, Autom. Constr. 144 (2022) 104591, http://dx.doi.org/10.1016/j.autcon.2022.104591, URL https://linkinghub.elsevier.com/retrieve/pii/S0926580522004617.

[6] T. DebRoy, H. Wei, J. Zuback, T. Mukherjee, J. Elmer, J. Milewski, A. Beese, A. Wilson-Heid, A. De, W. Zhang, Additive manufacturing of metallic components – process, structure and properties, Prog. Mater. Sci. 92 (2018) 112–224, http://dx.doi.org/10.1016/j.pmatsci.2017.10.001, URL https://linkinghub.elsevier.com/retrieve/pii/S0079642517301172.

[7] Q. Jia, D. Gu, Selective laser melting additive manufacturing of inconel 718 superalloy parts: Densification, microstructure and properties, J. Alloys Compd. 585 (2014) 713–721, http://dx.doi.org/10.1016/j.jallcom.2013.09.171, URL https://linkinghub.elsevier.com/retrieve/pii/S0925838813023451.

[8] W.H. Kan, L.N.S. Chiu, C.V.S. Lim, Y. Zhu, Y. Tian, D. Jiang, A. Huang, A critical review on the effects of process-induced porosity on the mechanical properties of alloys fabricated by laser powder bed fusion, J. Mater. Sci. 57 (21) (2022) 9818–9865, http://dx.doi.org/10.1007/s10853-022-06990-7, URL https://link.springer.com/10.1007/s10853-022-06990-7.

[9] H.M.A. Kolken, A.A. Zadpoor, Auxetic mechanical metamaterials, RSC Adv 7 (9) (2017) 5111–5129, http://dx.doi.org/10.1039/C6RA27333E, URL http://xlink.rsc.org/?DOI=C6RA27333E.

[10] X. Zheng, H. Lee, T.H. Weisgraber, M. Shusteff, J. DeOtte, E.B. Duoss, J.D. Kuntz, M.M. Biener, Q. Ge, J.A. Jackson, S.O. Kucheyev, N.X. Fang, C.M. Spadaccini, Ultralight, ultrastiff mechanical metamaterials, Science 344 (6190) (2014) 1373–1377, http://dx.doi.org/10.1126/science.1252291, URL https://www.science.org/doi/10.1126/science.1252291.

[11] F. Derveni, A.J. Gross, K.D. Peterman, S. Gerasimidis, Postbuckling behavior and imperfection sensitivity of elastic–plastic periodic plate-lattice materials, Extreme Mech. Lett. 50 (2022) 101510, http://dx.doi.org/10.1016/j.eml.2021.101510, URL https://linkinghub.elsevier.com/retrieve/pii/S2352431621001991.

[12] Y. Wang, X. Zhang, Z. Li, H. Gao, X. Li, Achieving the theoretical limit of strength in shell-based carbon nanolattices, Proc. Natl. Acad. Sci. 119 (34) (2022) e2119536119, http://dx.doi.org/10.1073/pnas.2119536119, URL https://pnas.org/doi/full/10.1073/pnas.2119536119.

[13] Z. Tao, X. Ren, L. Sun, Y. Zhang, W. Jiang, A.G. Zhao, Y.M. Xie, A novel re-entrant honeycomb metamaterial with tunable bandgap, Smart Mater. Struct. 31 (9) (2022) 095024, http://dx.doi.org/10.1088/1361-665X/ac812b, URL https://iopscience.iop.org/article/10.1088/1361-665X/ac812b.

[14] W. Cai, U.K. Chettiar, A.V. Kildishev, V.M. Shalaev, Optical cloaking with metamaterials, Nature Phot 1 (4) (2007) 224–227, http://dx.doi.org/10.1038/nphoton.2007.28, URL https://www.nature.com/articles/nphoton.2007.28.

[15] B. Li, Z. Huang, Y. Lin, X. Kang, Y. Li, Mechanical properties of novel folded kirigami metamaterials under quasi-static compression, Smart Mater. Struct. 31 (7) (2022) 075005, http://dx.doi.org/10.1088/1361-665X/ac68b4, URL https://iopscience.iop.org/article/10.1088/1361-665X/ac68b4.

[16] S. Babaee, J. Shim, J.C. Weaver, E.R. Chen, N. Patel, K. Bertoldi, 3D soft metamaterials with negative Poisson's ratio, Adv. Mater. 25 (36) (2013) 5044–5049, http://dx.doi.org/10.1002/adma.201301986, URL https://onlinelibrary.wiley.com/doi/10.1002/adma.201301986.

[17] T. Vitalis, A.J. Gross, S. Gerasimidis, Mechanical response and failure modes of three-dimensional auxetic re-entrant LPBF-manufactured steel truss lattice materials, J. Appl. Mech. (2024) 1–25, http://dx.doi.org/10.1115/1.4065669, URL https://asmedigitalcollection.asme.org/appliedmechanics/article/doi/10.1115/1.4065669/1200720/Mechanical-response-and-failure-modes-of-three.

[18] A. Vyatskikh, S. Delalande, A. Kudo, X. Zhang, C.M. Portela, J.R. Greer, Additive manufacturing of 3D nano-architected metals, Nature Commun. 9 (1) (2018) 593, http://dx.doi.org/10.1038/s41467-018-03071-9, URL http://www.nature.com/articles/s41467-018-03071-9.

[19] T.A. Schaedler, A.J. Jacobsen, A. Torrents, A.E. Sorensen, J. Lian, J.R. Greer, L. Valdevit, W.B. Carter, Ultralight metallic microlattices, Science 334 (6058) (2011) 962–965, http://dx.doi.org/10.1126/science.1211649, URL https://www.science.org/doi/10.1126/science.1211649.

[20] C. Crook, J. Bauer, A. Guell Izard, C. Santos de Oliveira, J. Martins de Souza e Silva, J.B. Berger, L. Valdevit, Plate-nanolattices at the theoretical limit of stiffness and strength, Nature Commun. 11 (1) (2020) 1579, http://dx.doi.org/10.1038/s41467-020-15434-2, URL http://www.nature.com/articles/s41467-020-15434-2.

[21] D. Mousanezhad, S. Babaee, H. Ebrahimi, R. Ghosh, A.S. Hamouda, K. Bertoldi, A. Vaziri, Hierarchical honeycomb auxetic metamaterials, Sci. Rep. 5 (1) (2016) 18306, http://dx.doi.org/10.1038/srep18306, URL http://www.nature.com/articles/srep18306.

[22] L.R. Meza, A.J. Zelhofer, N. Clarke, A.J. Mateos, D.M. Kochmann, J.R. Greer, Resilient 3D hierarchical architected metamaterials, Proc. Natl. Acad. Sci. 112 (37) (2015) 11502–11507, http://dx.doi.org/10.1073/pnas.1509120112, URL https://pnas.org/doi/full/10.1073/pnas.1509120112.

[23] M.-S. Pham, C. Liu, I. Todd, J. Lertthanasarn, Damage-tolerant architected materials inspired by crystal microstructure, Nature 565 (7739) (2019) 305–311, http://dx.doi.org/10.1038/s41586-018-0850-3, URL http://www.nature.com/articles/s41586-018-0850-3.

[24] M. Kheybari, C. Daraio, O.R. Bilal, Tunable auxetic metamaterials for simultaneous attenuation of airborne sound and elastic vibrations in all directions, Appl. Phys. Lett. 121 (8) (2022) 081702, http://dx.doi.org/10.1063/5.0104266, URL https://aip.scitation.org/doi/10.1063/5.0104266.

[25] R.E. Laureijs, J.B. Roca, S.P. Narra, C. Montgomery, J.L. Beuth, E.R.H. Fuchs, Metal additive manufacturing: Cost competitive beyond low volumes, J. Manuf. Sci. Eng. 139 (8) (2017) 081010, http://dx.doi.org/10.1115/1.4035420, URL https://asmedigitalcollection.asme.org/manufacturingscience/article/doi/10.1115/1.4035420/376354/Metal-Additive-Manufacturing-Cost-Competitive.

[26] UN, 2019 global status report for buildings and construction, 2019, URL https://globalabc.org/resources/flagship-products.

[27] UN, 2022 global status report for buildings and construction, 2022, URL https://globalabc.org/resources/flagship-products.

[28] G. De Schutter, K. Lesage, V. Mechtcherine, V.N. Nerella, G. Habert, I. Agusti-Juan, Vision of 3D printing with concrete — Technical, economic and environmental potentials, Cem. Concr. Res. 112 (2018) 25–36, http://dx.doi.org/10.1016/j.cemconres.2018.06.001, URL https://linkinghub.elsevier.com/retrieve/pii/S000888461731219X.

[29] J. Xiao, G. Ji, Y. Zhang, G. Ma, V. Mechtcherine, J. Pan, L. Wang, T. Ding, Z. Duan, S. Du, Large-scale 3D printing concrete technology: Current status and future opportunities, Cem. Concr. Compos. 122 (2021) 104115, http://dx.doi.org/10.1016/j.cemconcomp.2021.104115, URL https://linkinghub.elsevier.com/retrieve/pii/S0958946521001839.

[30] M.K. Mohan, A. Rahul, G. De Schutter, K. Van Tittelboom, Extrusion-based concrete 3D printing from a material perspective: A state-of-the-art review, Cem. Concr. Compos. 115 (2021) 103855, http://dx.doi.org/10.1016/j.cemconcomp.2020.103855, URL https://linkinghub.elsevier.com/retrieve/pii/S0958946520303607.

[31] J. Zhang, J. Wang, S. Dong, X. Yu, B. Han, A review of the current progress and application of 3D printed concrete, Composites A 125 (2019) 105533, http://dx.doi.org/10.1016/j.compositesa.2019.105533, URL https://linkinghub.elsevier.com/retrieve/pii/S1359835X19302829.

[32] R. Buswell, W. Leal De Silva, S. Jones, J. Dirrenberger, 3D printing using concrete extrusion: A roadmap for research, Cem. Concr. Res. 112 (2018) 37–49, http://dx.doi.org/10.1016/j.cemconres.2018.05.006, URL https://linkinghub.elsevier.com/retrieve/pii/S0008884617311924.

[33] D. Asprone, F. Auricchio, C. Menna, V. Mercuri, 3D printing of reinforced concrete elements: Technology and design approach, Constr. Build. Mater. 165 (2018) 218–231, http://dx.doi.org/10.1016/j.conbuildmat.2018.01.018, URL https://linkinghub.elsevier.com/retrieve/pii/S0950061818300187.

[34] B. Panda, S.C. Paul, N.A.N. Mohamed, Y.W.D. Tay, M.J. Tan, Measurement of tensile bond strength of 3D printed geopolymer mortar, Measurement 113 (2018) 108–116, http://dx.doi.org/10.1016/j.measurement.2017.08.051, URL https://linkinghub.elsevier.com/retrieve/pii/S0263224117305560.

[35] A. Douba, P. Badjatya, S. Kawashima, Enhancing carbonation and strength of MgO cement through 3D printing, Constr. Build. Mater. 328 (2022) 126867, http://dx.doi.org/10.1016/j.conbuildmat.2022.126867, URL https://linkinghub.elsevier.com/retrieve/pii/S0950061822005530.

[36] J. Burger, E. Lloret-Fritschi, F. Scotto, T. Demoulin, L. Gebhard, J. Mata-Falcón, F. Gramazio, M. Kohler, R.J. Flatt, Eggshell: Ultra-thin three-dimensional printed formwork for concrete structures, 3D Printing and Addit. Manuf 7 (2) (2020) 48–59, http://dx.doi.org/10.1089/3dp.2019.0197, URL https://www.liebertpub.com/doi/10.1089/3dp.2019.0197.

[37] G. Tzortzinis, A. Gross, S. Gerasimidis, Auxetic boosting of confinement in mortar by 3D reentrant truss lattices for next generation steel reinforced concrete members, Extreme Mech. Lett. 52 (2022) 101681, http://dx.doi.org/10.1016/j.eml.2022.101681, URL https://linkinghub.elsevier.com/retrieve/pii/S2352431622000438.

[38] B. Salazar, P. Aghdasi, I.D. Williams, C.P. Ostertag, H.K. Taylor, Polymer lattice-reinforcement for enhancing ductility of concrete, Mater. Des. 196 (2020) 109184, http://dx.doi.org/10.1016/j.matdes.2020.109184, URL https://linkinghub.elsevier.com/retrieve/pii/S026412752030719X.

[39] Y. Xu, H. Zhang, E. Schlangen, M. Luković, B. Šavija, Cementitious cellular composites with auxetic behavior, Cem. Concr. Compos. 111 (2020) 103624, http://dx.doi.org/10.1016/j.cemconcomp.2020.103624, URL https://linkinghub.elsevier.com/retrieve/pii/S0958946520301165.

[40] Y. Xu, H. Zhang, Y. Gan, B. Šavija, Cementitious composites reinforced with 3D printed functionally graded polymeric lattice structures: Experiments and modelling, Addit. Manuf. 39 (2021) 101887, http://dx.doi.org/10.1016/j.addma.2021.101887, URL https://linkinghub.elsevier.com/retrieve/pii/S221486042100052X.

[41] V. Nguyen-Van, J. Liu, S. Li, G. Zhang, H. Nguyen-Xuan, P. Tran, Modelling of 3D-printed bio-inspired bouligand cementitious structures reinforced with steel fibres, Eng. Struct. 274 (2023) 115123, http://dx.doi.org/10.1016/j.engstruct.2022.115123, URL https://linkinghub.elsevier.com/retrieve/pii/S0141029622011993.

[42] W. Ritter, Die Bauweise Hennebique, Schweizerische Bauzeitung Bd XXXIII (7) (1899).

[43] E. Mörsch, Der Eisenbeton, seine Theorie und Anwenung, Verlag Konrad Witter, 1912.

[44] J. Schlaich, K. Schäfer, Design and detailing of structural concrete using strut-and-tie models, The Struct. Eng 69 (6) (1991).

[45] P. Marti, Basic tools of reinforced concrete beam design, ACI J., Proceedings, V. 82, No. 1, Jan.-Feb. 1985 (1985) 46–56.

[46] F.E. Richart, A. Brandtzaeg, R.L. Brown, Failure of Plain and Spirally Reinforced Concrete in Compression, 190, University of Illinois Engineering experiment station, 1929.

[47] D.C. Kent, R. Park, Flexural members with confined concrete, J. Struct. Div. 97 (7) (1971) 1969–1990, http://dx.doi.org/10.1061/JSDEAG.0002957, URL https://ascelibrary.org/doi/10.1061/JSDEAG.0002957.

[48] S.A. Sheikh, S.M. Uzumeri, Strength and ductility of tied concrete columns, J. Struct. Div. 106 (5) (1980) 1079–1102, http://dx.doi.org/10.1061/JSDEAG.0005416, URL https://ascelibrary.org/doi/10.1061/JSDEAG.0005416.

[49] R. Park, M.J.N. Priestley, W.D. Gill, Ductility of square-confined concrete columns, J. Struct. Div. 108 (4) (1982) 929–950, http://dx.doi.org/10.1061/JSDEAG.0005933, URL https://ascelibrary.org/doi/10.1061/JSDEAG.0005933.

[50] J.B. Mander, M.J.N. Priestley, R. Park, Observed stress-strain behavior of confined concrete, J. Struct. Eng. 114 (8) (1988) 1827–1849, http://dx.doi.org/10.1061/(ASCE)0733-9445(1988)114:8(1827).

[51] J.B. Mander, M.J.N. Priestley, R. Park, Theoretical stress-strain model for confined concrete, J. Struct. Eng. 114 (8) (1988) 1804–1826, http://dx.doi.org/10.1061/(ASCE)0733-9445(1988)114:8(1804).

[52] M. Saatcioglu, S.R. Razvi, Strength and ductility of confined concrete, J. Struct. Eng. 118 (6) (1992) 1590–1607, http://dx.doi.org/10.1061/(ASCE)0733-9445(1992)118:6(1590).

[53] C. Lu, M. Hsieh, Z. Huang, C. Zhang, Y. Lin, Q. Shen, F. Chen, L. Zhang, Architectural design and additive manufacturing of mechanical metamaterials: A review, Engineering (2022) http://dx.doi.org/10.1016/j.eng.2021.12.023, URL https://linkinghub.elsevier.com/retrieve/pii/S2095809922003654, S2095809922003654.

[54] B. Schagen, Upscaling architected metamaterials for applications in civil infrastructure: auxetic lattices for confining concrete, Master's Thesis, TU Delft, 2023.

[55] Q.Q. Liang, Y.M. Xie, G.P. Steven, Topology optimization of strut-and-tie models in reinforced concrete structures using an evolutionary procedure, ACI Struct. J 97 (2) (2000) http://dx.doi.org/10.14359/863, URL http://www.concrete.org/Publications/ACIMaterialsJournal/ACIJournalSearch.aspx?m=details&ID=863.

[56] M. Zheng-Dong, Three-dimensional auxetic structures and applications thereof, (2010/01 19792 A1) 2010.

[57] D. Photiou, S. Avraam, F. Sillani, F. Verga, O. Jay, L. Papadakis, Experimental and numerical analysis of 3D printed polymer tetra-petal auxetic structures under compression, Appl. Sci. 11 (21) (2021) 10362, http://dx.doi.org/10.3390/app112110362, URL https://www.mdpi.com/2076-3417/11/21/10362.

[58] Y. Chen, M.-H. Fu, A novel three-dimensional auxetic lattice meta-material with enhanced stiffness, Smart Mater. Struct. 26 (10) (2017) 105029, http://dx.doi.org/10.1088/1361-665X/aa819e, URL https://iopscience.iop.org/article/10.1088/1361-665X/aa819e.

[59] V. Lvov, F. Senatov, A. Korsunsky, A. Salimon, Design and mechanical properties of 3D-printed auxetic honeycomb structure, Mater. Today Commun. 24 (2020) 101173, http://dx.doi.org/10.1016/j.mtcomm.2020.101173, URL https://linkinghub.elsevier.com/retrieve/pii/S2352492820307637.

[60] T.-C. Lim, A 3D auxetic material based on intersecting double arrowheads: A 3D auxetic material based on intersecting double arrowheads, Phys. Status Solidi (b) 253 (7) (2016) 1252–1260, http://dx.doi.org/10.1002/pssb.201600015, URL https://onlinelibrary.wiley.com/doi/10.1002/pssb.201600015.

[61] L. Yang, O. Harrysson, H. West, D. Cormier, Mechanical properties of 3D re-entrant honeycomb auxetic structures realized via additive manufacturing, Int. J. Solids Struct. 69–70 (2015) 475–490, http://dx.doi.org/10.1016/j.ijsolstr.2015.05.005, URL https://linkinghub.elsevier.com/retrieve/pii/S0020768315002152.

[62] W. Zhang, Z. Li, J. Wang, F. Scarpa, X. Wang, Mechanics of novel asymmetrical re-entrant metamaterials and metastructures, Compos. Struct. 291 (2022) 115604, http://dx.doi.org/10.1016/j.compstruct.2022.115604, URL https://linkinghub.elsevier.com/retrieve/pii/S0263822322003907.

[63] J.C. Álvarez Elipe, A. Díaz Lantada, Comparative study of auxetic geometries by means of computer-aided design and engineering, Smart Mater. Struct. 21 (10) (2012) 105004, http://dx.doi.org/10.1088/0964-1726/21/10/105004, URL https://iopscience.iop.org/article/10.1088/0964-1726/21/10/105004.

[64] G. Zhou, Z.-D. Ma, G. Li, A. Cheng, L. Duan, W. Zhao, Design optimization of a novel NPR crash box based on multi-objective genetic algorithm, Struct. Multidiscip. Optim. 54 (3) (2016) 673–684, http://dx.doi.org/10.1007/s00158-016-1452-z, URL http://link.springer.com/10.1007/s00158-016-1452-z.

[65] L. Zhang, B. Wang, B. Song, Y. Yao, S.-K. Choi, C. Yang, Y. Shi, 3D printed biomimetic metamaterials with graded porosity and tapering topology for improved cell seeding and bone regeneration, Bioactive Materials (2022) http://dx.doi.org/10.1016/j.bioactmat.2022.07.009, URL https://linkinghub.elsevier.com/retrieve/pii/S2452199X22003085, S2452199X22003085.

[66] H. Kolken, S. Callens, M. Leeflang, M. Mirzaali, A. Zadpoor, Merging strut-based and minimal surface meta-biomaterials: Decoupling surface area from mechanical properties, Addit. Manuf. 52 (2022) 102684, http://dx.doi.org/10.1016/j.addma.2022.102684, URL https://linkinghub.elsevier.com/retrieve/pii/S2214860422000896.

[67] B.D. Scott, R. Park, M.J.N. Priestley, Stress-strain behavior of concrete confined by overlapping Hoops at low and high strain rates, ACI J. Proc 79 (1) (1982) http://dx.doi.org/10.14359/10875, URL http://www.concrete.org/Publications/ACIMaterialsJournal/ACIJournalSearch.aspx?m=details&ID=10875.

[68] S.J. Foster, M.M. Attard, Strength and ductility of fiber-reinforced high-strength concrete columns, J. Struct. Eng. 127 (1) (2001) 28–34, http://dx.doi.org/10.1061/(ASCE)0733-9445(2001)127:1(28), URL https://ascelibrary.org/doi/10.1061/%28ASCE%290733-9445%282001%29127%3A1%2828%29.

[69] H.O. Shin, Y.S. Yoon, W.D. Cook, D. Mitchell, Effect of confinement on the axial load response of ultrahigh-strength concrete columns, J. Struct. Eng. 141 (6) (2015) 04014151, http://dx.doi.org/10.1061/(ASCE)ST.1943-541X.0001106, URL https://ascelibrary.org/doi/10.1061/%28ASCE%29ST.1943-541X.0001106.

[70] SIMULIA Abaqus/Standard CAE 2023, Dassault Systèmes, 2022, URL https://www.3ds.com/products-services/simulia/products/abaqus/abaquscae/.

[71] Q.-S. Yang, W. Becker, Numerical investigation for stress, strain and energy homogenization of orthotropic composite with periodic microstructure and non-symmetric inclusions, Comput. Mater. Sci. 31 (1–2) (2004) 169–180.

[72] Z. Hashin, S. Shtrikman, A variational approach to the theory of the elastic behaviour of multiphase materials, J. Mech. Phys. Solids 11 (2) (1963) 127–140, http://dx.doi.org/10.1016/0022-5096(63)90060-7, URL https://linkinghub.elsevier.com/retrieve/pii/0022509663900607.

[73] C01 Committee, Test method for compressive strength of hydraulic cement mortars (using 2-in. or [50mm] Cube Specimens), ASTM International, URL http://www.astm.org/cgi-bin/resolver.cgi?C109C109M-21.

[74] Rhino 3D v7, Robert McNeel & Associates (TLM, Inc.), 2020, URL https://www.rhino3d.com/.
[75] Solidworks 3D CAD Design 2023, Dassault Systèmes, 2022, URL https://www.solidworks.com/.
[76] A.I. Marques, J. Morais, P. Morais, M.D.R. Veiga, C. Santos, P. Candeias, J.G. Ferreira, Modulus of elasticity of mortars: Static and dynamic analyses, Constr. Build. Mater. 232 (2020) 117216, http://dx.doi.org/10.1016/j.conbuildmat.2019.117216, URL https://linkinghub.elsevier.com/retrieve/pii/S0950061819326686.
[77] A.M. Roach, B.C. White, A. Garland, B.H. Jared, J.D. Carroll, B.L. Boyce, Size-dependent stochastic tensile properties in additively manufactured 316l stainless steel, Addit. Manuf. 32 (2020) 101090, http://dx.doi.org/10.1016/j.addma.2020.101090, URL https://linkinghub.elsevier.com/retrieve/pii/S2214860419315738.
[78] C01 Committee, Practice for mechanical mixing of hydraulic cement pastes and mortars of plastic consistency, ASTM International, URL http://www.astm.org/cgi-bin/resolver.cgi?C305-20.
[79] ASTM, C128-22 test method for relative density (specific gravity) and absorption of fine aggregate, ASTM International, URL http://www.astm.org/cgi-bin/resolver.cgi?C128-22.
[80] P.K. Kolay, S.O. Sulaiman, S. Kumar, Freeze-thaw durability of concrete with natural and recycled concrete aggregates using air-entraining admixture, Adv. Civil Eng Mater 7 (3) (2018) 328–346, http://dx.doi.org/10.1520/ACEM20170079, URL https://asmedigitalcollection.asme.org/civilengineeringmaterials/article/7/3/328/1173445/Freeze-Thaw-Durability-of-Concrete-with-Natural.
[81] S.J. Foster, M.M. Attard, Experimental tests on eccentrically loaded high strength concrete columns, ACI Struct. J 94 (3) (1997) http://dx.doi.org/10.14359/481, URL http://www.concrete.org/Publications/ACIMaterialsJournal/ACIJournalSearch.aspx?m=details&ID=481.
[82] V. Deshpande, M. Ashby, N. Fleck, Foam topology: bending versus stretching dominated architectures, Acta Mater. 49 (6) (2001) 1035–1040, http://dx.doi.org/10.1016/S1359-6454(00)00379-7, URL https://linkinghub.elsevier.com/retrieve/pii/S1359645400003797.
[83] J. Carlsson, A. Kuswoyo, A. Shaikeea, N. Fleck, Compression of filled, open-cell, 3D-printed Kelvin lattices, Mech. Mater. 188 (2024) 104851, http://dx.doi.org/10.1016/j.mechmat.2023.104851, URL https://linkinghub.elsevier.com/retrieve/pii/S0167663623002971.
[84] R.F. Zollo, Fiber-reinforced concrete: an overview after 30 years of development, Cem. Concr. Compos. 19 (2) (1997) 107–122, http://dx.doi.org/10.1016/S0958-9465(96)00046-7, URL https://linkinghub.elsevier.com/retrieve/pii/S0958946596000467.
[85] V. Afroughsabet, L. Biolzi, T. Ozbakkaloglu, High-performance fiber-reinforced concrete: a review, J. Mater. Sci. 51 (14) (2016) 6517–6551, http://dx.doi.org/10.1007/s10853-016-9917-4, URL http://link.springer.com/10.1007/s10853-016-9917-4.
[86] Eurocode 3: design of steel structures. Part 1-8: Design of joints, BSI, OCLC, (2010) 975150089.
[87] P. Paultre, F. Légeron, Confinement reinforcement design for reinforced concrete columns, J. Struct. Eng. 134 (5) (2008) 738–749, http://dx.doi.org/10.1061/(ASCE)0733-9445(2008)134:5(738), URL https://ascelibrary.org/doi/10.1061/%28ASCE%290733-9445%282008%29134%3A5%28738%29.